

THE BENEFIT OF SIMULTANEOUS SEVEN-FILTER IMAGING:  
10 YEARS OF GROND OBSERVATIONS

J. GREINER<sup>1</sup>

<sup>1</sup>*Max-Planck-Institut für extraterrestrische Physik, 85740 Garching, Germany*

ABSTRACT

A variety of scientific results have been achieved over the last 10 years with the GROND simultaneous 7-channel imager at the 2.2m telescope of the Max-Planck Society at ESO/La Silla. While designed primarily for rapid observations of gamma-ray burst afterglows, the combination of simultaneous imaging in the Sloan  $g'r'i'z'$  and near-infrared  $JHK_s$  bands at a medium-sized (2.2m) telescope and the very flexible scheduling possibility has resulted in an extensive use for many other astrophysical research topics, from exoplanets and accreting binaries to galaxies and quasars.

*Keywords:* instrumentation: detectors, techniques: photometric

arXiv:1812.00636v1 [astro-ph.HE] 3 Dec 2018

## 1. INTRODUCTION

An increasing number of scientific questions require the measurement of spatially and spectrally resolved intensities of radiation from astrophysical objects. Over the last decade, transient and time-variable sources are increasingly moving in the focus of present-day research (with its separate naming of “time-domain astronomy”), recently boosted spectacularly by the follow-up of gravitational wave sources. If the spatial scale of such a study is small (few arcmin), integral field spectrographs such as PMAS (3.6m Calar Alto) or MUSE (VLT) or ESI/OSIRIS (Keck) are the instruments of choice. If crowding is not an issue, (objective) prism spectroscopy is a valuable option (Teplitz et al. 2000). For large scales, simultaneous multi-channel imaging is applied. The physical measurement goals often request a compromise between spatial, temporal or spectral resolution, which adds to the challenges of the measurement principle.

Simultaneous imaging in different filter-bands (whether Johnson *UBVR<sub>I</sub>JHK* or Sloan *u'g'r'i'z'* or anything else) is of interest in a variety of astrophysical themes. The primary aim is to measure the spectral energy distribution (SED) or its evolution in variable astrophysical objects, in order to uncover the underlying emission mechanism. Examples are, among others, (1) monitoring of all kinds of variable stars (flare stars, cataclysmic variables, X-ray binaries) to determine the outburst mechanisms and differentiate between physical state changes and changes induced by geometrical variations, like eclipses; (2) follow-up of gamma-ray burst (GRB) afterglows for e.g. rapid redshift estimates, mapping the SED evolution to measure circumburst parameters, or the search for dust destruction; (3) monitoring of AGN to understand the physical origin of the observed variability; (4) determining the inclination of X-ray heated binaries (Orosz & Bailyn 1997);

(5) mapping of galaxies to study their stellar population; (6) multi-color light curves of supernovae to, e.g., recognize dust formation (Taubenberger et al. 2006); (7) differentiating achromatic microlensing events (Paczynski 1986) from other variables with similar light curves; (8) identifying objects with peculiar SEDs, e.g. photometric redshift surveys for high-*z* active galactic nuclei, or identifying brown dwarfs; (9) observations of transiting extrasolar planets to infer orbital periods, multiplicity of planets, or characteristics of their atmospheres (Jha et al. 2000); or (10) mapping of reflectance of solar system bodies as a function of their rotation to map their surface chemical composition (Jewitt 2002).

Instruments with simultaneous imaging capability in different filter bands prior to the GROND development include ANDICAM (Depoy 1998), BUSCA (Reif et al. 1999), HIPO (Dunham et al. 2004), MITSuME (Kotani et al. 2005), TRISPEC (Watanabe et al. 2005), SQUIID (Ellis et al. 1993), and ULTRACAM (Dhillon et al. 2007). GROND-inspired instruments include the 6-channel RATIR (Butler et al. 2012) and the 4-channel ROS2 (Spano et al. 2010) instruments. Further projects for simultaneous multi-band instruments are the 8-channel OCTOCAM (Gorosabel & Ugarte Postigo 2010), selected as part of the Gemini instrumentation program in 2017 (Roming et al. 2018), the 4-channel SPARC4 (Rodrigues et al. 2012) planned for installation at the 1.6 m telescope of the Pico dos Dias Observatory (Brazil) (Bernardes et al. 2018), an unnamed 8-channel imager for the IRTF (Connelley et al. 2013), and the SIOUX project (Christille et al. 2016). In comparison, the GROND instrument (Greiner et al. 2008) at the 2.2 m telescope of the Max-Planck Society (MPG) in La Silla (ESO/Chile) with its 7 simultaneous channels so far still delivers the largest degree of multiplexing at such a telescope size.

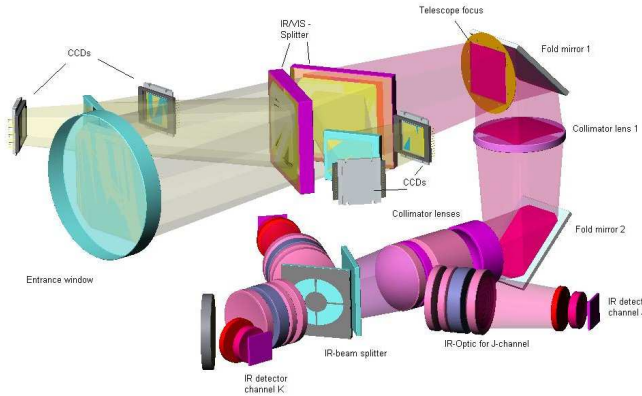


**Figure 1.** Scheme of the optical beam path of GROND with the optical components and the detectors labeled. [From Greiner et al. (2008)] ©AAS. Reproduced with permission.

After a short description of the main features of the instrument and operational aspects (§2), I describe some of our prime scientific results obtained via GROND observations, foremost for GRBs (§3) and transients (§4), but also other science topics where color information on short timescales is important (§5 – 9). While this is predominantly a review, it contains hitherto unpublished results, e.g. on the discovery of a hitherto unknown T5 brown dwarf.

## 2. THE GROND INSTRUMENT AND ITS OPERATION

The primary goal was to rapidly identify GRB afterglows and measuring their redshift. This led to the concept of a camera which allows simultaneous observations in multiple filters throughout the optical and near-infrared region. The simultaneity is dictated by the fact that a typical GRB afterglow initially fades by about 2–3 mag within 5–10 min after the GRB, and by another 3 mag in the following 50 min, thus rendering cycling through different filters useless. Furthermore, with the advent of *Swift*'s detection of  $\sim 100$  GRBs/yr, follow-up of each GRB with an 8 m telescope became impractical, and some knowledge-based pre-selection was needed. Four bands were implemented in

the visual, plus three (standard  $JHK_s$ ) bands in the near-infrared (NIR). The separation of the different photometric bands was achieved using dichroic beamsplitters (in the converging beam), whereby the short wavelength part of the light is always reflected off the dichroic, while the long-wavelength part passes through (Fig. 1). The use of dichroics implies that adjacent bands do have identical 50% transmission wavelengths, making the Sloan filter system (Fukugita et al. 1996) the obvious choice for the visual bands.

The field-of-view (FOV) of the camera was designed, on one hand, to cover the typical few arcmin extent of GRB error boxes, and on the other hand have a pixel scale less than the mean seeing to allow for accurate photometry. Mounted at the MPG-owned 2.2 m diameter f/8 telescope on La Silla (ESO/Chile) with an intrinsic image quality of  $0''.4$ , the FOV of each visual band is  $5.4 \times 5.4$  arcmin<sup>2</sup>, (2048x2048 CCD with plate scale  $0''.158/\text{pixel}$ ), and  $10 \times 10$  arcmin<sup>2</sup> in the NIR using a focal reducer ( $1024 \times 1024$  Rockwell HAWAII-1 array with a plate scale of  $0''.60/\text{pixel}$ ). A Sumitomo closed-cycle cooler provides a temperature of 65 K for the NIR detectors and 80 K for the focal reducer optics, with simple damping preventing any telescope/instrument vibrations which could degrade the image quality. The best GROND images have a full-width-half-maximum of  $0''.6$ , dominated by the dome seeing. This allows us to linearly increase sensitivity by adding more exposure (stacking) up to 3–4 hrs, before becoming background-dominated (see, e.g. Fig. 2).

The standard detector readout systems which were used at ESO at the time were implemented, i.e. FIERA (Beletic et al. 1998) for the visual channels, and IRACE (Meyer et al. 1998) for the NIR channels. This makes for a very flexible readout scheme, where e.g. NIR exposures continue during the CCD-readout. Since

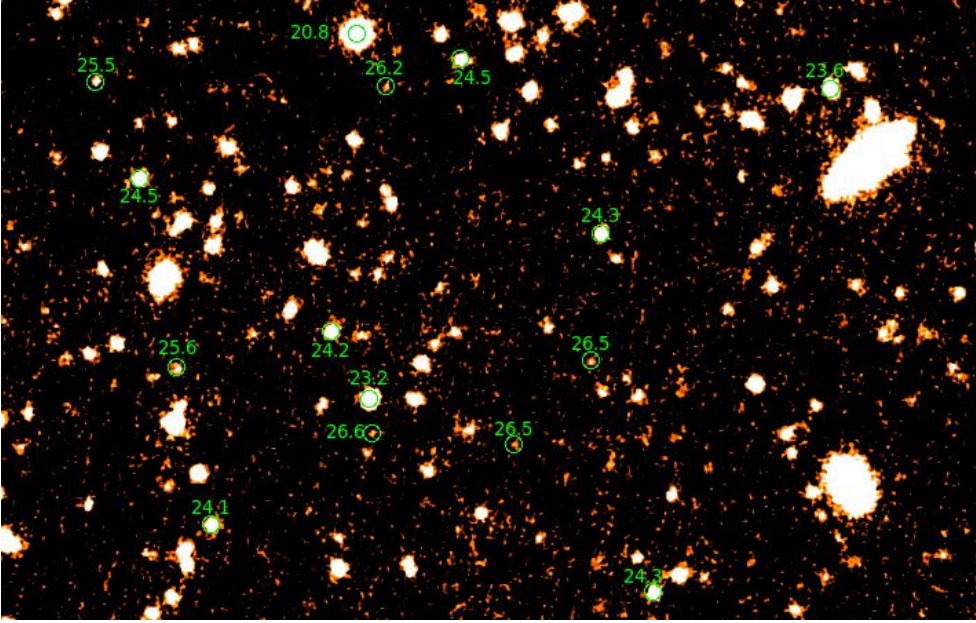


**Figure 2.** An example for the sensitivity of GROND@2.2m, reaching  $g' = 26.5$  mag in 3.5 hrs exposure time (Yates et al. 2015), likely one of the deepest images from a ground-based 2 m class telescope. The green numbers are SDSS-calibrated  $g'$ -magnitudes. This  $g'$ -band image is  $1'.1 \times 1'.8$ ; North is up, and East to the left.

the  $JHK_s$  channels operate fully synchronously, a 10 s exposure was adopted as a compromise between not saturating the  $K_s$ -band while maximizing  $J$ -band exposure per telescope dither position. In addition, a separate internal dither mechanism was implemented in the  $K_s$ -band; full details can be found in Greiner et al. (2008).

While originally foreseen to only operate in robotic target-of-opportunity mode for chasing GRB afterglows, the GROND operation scheme was designed flexibly enough to allow also visitor-mode style “manual” observations. All parameters for GROND observations can be adapted through standard ESO-style observation blocks (OBs) which are used for all observations, whether visitor/service mode or robotic. Normal observing program observers use the canonical p2pp tool (P2PP Manual 2007<sup>1</sup>), while in the case of GRB observations, OBs are generated in real-time by an automatic process. A special commandable mirror allows to switch between GROND and the other two 2.2 m instruments (WFI, FEROS) within 20 s.

<sup>1</sup> see [www.eso.org/observing/p2pp/P2PP-tool.html#Manual](http://www.eso.org/observing/p2pp/P2PP-tool.html#Manual)

At the start of each OB, the instrument is automatically focused by moving the telescope’s secondary mirror.

Best possible instrument efficiency has been the main driver during the design and development of GROND. As a result, the total efficiency in the visual bands is about 70% (except the  $z'$  band), and is still above 50% for the three NIR bands (Greiner et al. 2008), despite the eleven lenses per channel and the comparatively low quantum efficiency of the 2001-built HAWAII detectors. Thus, even in a single filter, GROND is the most sensitive instrument at a 2 m-class telescope. Due to the simultaneous imaging in 7 channels, GROND is likely the instrument with the highest photon-detection efficiency in the 0.4–2.5  $\mu\text{m}$  band.

GROND was commissioned at the MPG 2.2 m telescope at La Silla (ESO, Chile) in April/May 2007, and the first gamma-ray burst followed up was GRB 070521 (Greiner et al. 2007). For the first few months (until end of September 2007), follow-up observations depended on the willingness of the scheduled observers to share observing time. Thereafter, weather permitting, a general override permission and a 15% share of total telescope time allowed us to fol-



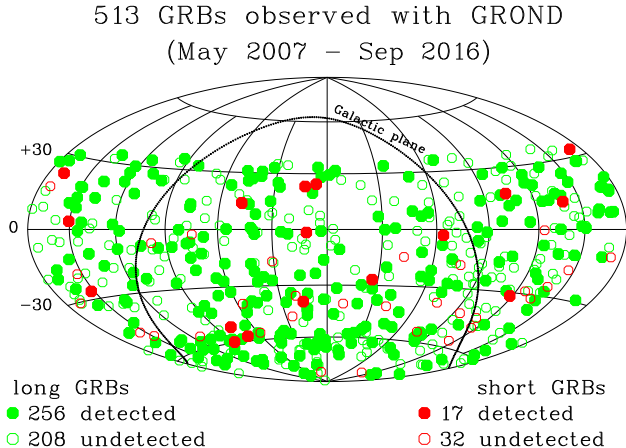


**Figure 3.** Sky distribution in equatorial coordinates of the GROND GRB sample.

low every well-localized GRB which was visible from La Silla, with only few exceptions. A MPE directorial decision terminated this systematic GRB follow-up program with GROND at the beginning of October 2016.

### 3. GAMMA-RAY BURSTS

#### 3.1. Long- and short-duration GRBs

GRBs are the most luminous electromagnetic sources on the sky, releasing in less than a minute the energy output of the Sun over its entire life. GRBs form two sub-groups according to their duration: (i) Long-duration GRBs ( $>2$  s) are firmly linked to the collapse of massive stars (Hjorth et al. 2003; Stanek et al. 2003), thus probing sites of star formation with little delay, as the star’s lifetimes are measured in megayears. GRBs have been seen up to the highest measured redshifts. (ii) Short-duration GRBs are commonly believed to originate from the merging of compact stars, as verified by the recent detection of gravitational waves from GRB 170817A (Abbott et al. 2017b).

Present  $\gamma$ -ray instrumentation provides a detection rate of about one GRB per day, and thus GRBs act as frequently available signposts throughout the Universe. Over the last 2 decades, these ultra-luminous cosmological ex-

plosions have been transformed from a mere curiosity to essential tools for the study of high-redshift stars and galaxies, early structure formation and the evolution of chemical elements.

#### 3.2. GROND Observing statistics

A total of 842 GRBs were promptly localized by the Neil Gehrels *Swift* Observatory and 301 by other missions<sup>2</sup> (the majority with error boxes much larger than the  $10'$  of GROND) between May 2007 and September 2016. 879 of these happened at declination smaller than  $+36^{\text{d}}5$  (which is about the northern-most declination reachable with GROND due to a minimum  $20^\circ$  horizon distance requirement of the 2.2m telescope), out of which 513 were followed-up with GROND. 256 of the 464 long-duration GRBs were detected, and 17 of the 49 short-duration GRBs (Fig. 3). For the subset of 709 *Swift*-detected GRBs with immediately (up to few hours) well-localized *Swift*/XRT afterglow positions, 532 were observable for GROND, and 439 were actually observed. This implies a follow-up efficiency of these well-localized *Swift*-GRBs of 82%, with bad weather periods and main-mirror coating events being the largest impact factors among the not-observed sources.

#### 3.3. GRBs as high-redshift probes

GROND operations started very promising: about 1 year after commissioning, the afterglow of GRB 080913 at  $z=6.7$  (see Fig. 4) was discovered with GROND (Greiner et al. 2009a), and spectroscopically confirmed with ESO/VLT spectroscopy. This served as the “proof-of-concept” for using simultaneous multi-band photometry of GRB afterglows to accurately measure photometric redshifts. Later on, GROND significantly contributed to the record-breaking GRBs 090423 (Tanvir et al. 2009) and 090429B (Cucchiara et al. 2011) by providing

<sup>2</sup> see <http://mpe.mpg.de/~jcg/grbgen.html> for a complete list

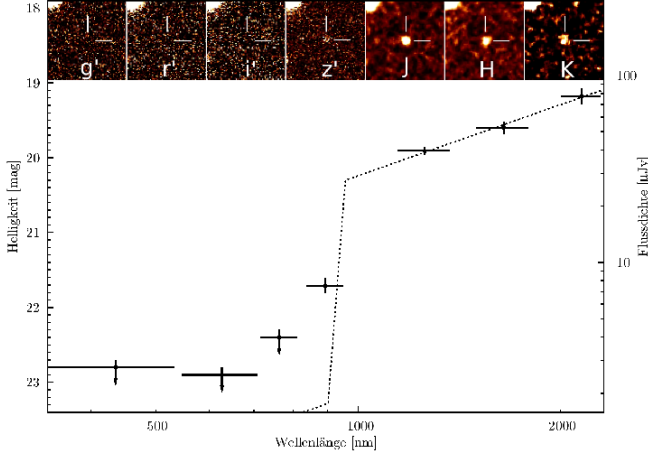


**Figure 4.** GROND spectral energy distribution and the corresponding image cut-outs (top row) for GRB 080913 at  $z=6.7$  (Greiner et al. 2009a). The GROND observation started about 6 min after the Swift/BAT trigger, and the photometric redshift was available 35 min after the trigger, formed from the stack of the first 3 OBs. This information was used to trigger FORS spectroscopy at ESO/VLT which confirmed the GROND photo- $z$  to be accurate to within 5% [From Greiner et al. (2009a)]. ©AAS. Reproduced with permission.

data for additional filters or allowing to calibrate the typically small field-of-view NIR instruments on the 8-10m telescopes.

Among 273 GRB afterglows detected with GROND, we have not found a single GRB afterglow with only a  $HK_s$  detection, i.e. a  $J$ -band drop-out. Unless  $z > 10$  GRBs are systematically underluminous, and thus below the GROND threshold ( $H(AB) > 21$  mag,  $K_S(AB) > 20$  mag in one hour exposure), the relative frequency of such  $z > 10$  GRBs is below 0.4% ( $1\sigma$ ). This is consistent with recent predictions of the redshift distribution of GRBs, similar to our earlier estimate (Greiner et al. 2011) of  $\sim 5\%$  of GRBs at  $z > 5$  (e.g. Elliott et al. 2012; Le & Mehta 2017).

### 3.4. Dust and Dark GRBs

Soon after the discovery of GRB afterglows it became clear that the detection rate in the optical wavelength range was substantially lower

than that in X-rays (e.g. Groot et al. 1998; Kloise et al. 2000; Djorgovski et al. 2001). The reasons for the occurrence of such “dark” bursts were first discussed systematically in Fynbo et al. (2001) and Lazzati, Covino, Ghisellini (2002). These involve (i) either an intrinsically low luminosity, e.g. an optically bright vs. optically dark dichotomy, or (ii) a large extinction by intervening material, either very locally around the GRB, or along the line-of-sight through the host galaxy, or (iii) high redshift ( $z > 5 - 6$ ), so that Ly $\alpha$  blanketing and absorption by the intergalactic medium would prohibit detection in the frequently used  $R$  band (Lamb & Reichart 2000). A sample of 39 long-duration GRB afterglows, complete in observational bias and redshift, and observed with GROND within 4 hrs, established the fraction of dark bursts to be  $18 \pm 8\%$ . Among these dark bursts, the different shape of the spectral energy distribution allows us to differentiate between two options:  $57 \pm 14\%$  are due to moderate dust extinction enhanced due to moderate redshift, while  $28 \pm 14\%$  are due to flux depression because of high redshift,  $z > 5$  (Greiner et al. 2011). Since the afterglow detection rate of this sample was very high (92%; just three GRB afterglows missed) the above errors also include potential intrinsically faint GRBs, where the maximum brightness during the first 4 hrs after the GRB was below the sensitivity threshold of GROND@2.2m.

Another early and surprising result was the very dusty GRB 070802 at a redshift of  $z = 2.45$ . The SED deviated clearly from the typical synchrotron power law shape, showing increasing curvature towards the bluest band and a low-flux ‘outlier’ in the  $i'$ -band (Fig. 5). We interpreted the  $i'$ -band drop as extinction by the 2175 Å feature, redshifted in the GRB host galaxy (Krühler et al. 2008). This was one of the first and clearest detections of the 2175 Å feature at high redshift, and was later confirmed

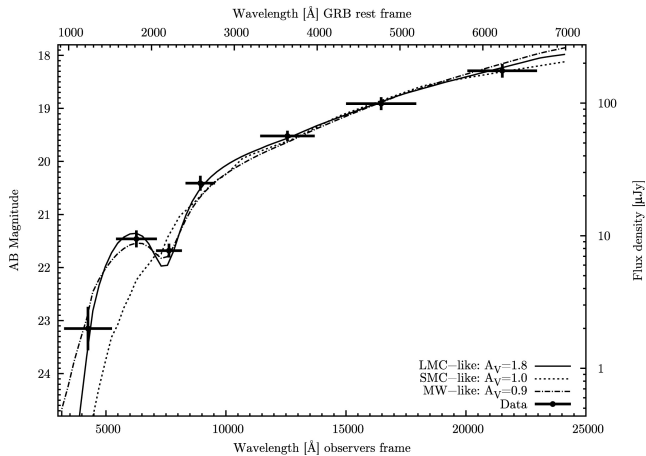


**Figure 5.** GROND  $g'r'i'z'JHK_s$  spectral energy distribution of the afterglow of GRB 070802, showing a clear drop of the  $i'$ -band, interpreted as the redshifted 2175 Å bump in the GRB host galaxy [From Krühler et al. (2008)]. ©AAS. Reproduced with permission.

by optical spectroscopy (Eliasdóttir et al. 2009) with VLT/X-shooter.

Motivated by these examples of strong host-intrinsic extinction and the availability of our unique GROND sample of dusty GRBs, a search for (Rossi et al. 2012), or detailed analysis (Krühler et al. 2011b) of their host galaxies has been undertaken. This revealed systematic differences in their properties relative to the hosts of optically bright GRBs: they are systematically redder, more luminous and more massive, suggesting chemically evolved hosts (Krühler et al. 2011b). This finding established that the dust along the sight-line of GRBs is often related to global host properties, and thus not located in the immediate GRB environment as expected for a massive star dying within its star forming region. By now, this correlation is well accepted, and used in an inverted way to search for infrared-bright host galaxies of GRBs without optical afterglow, in order to obtain redshifts and host details (Chrimes et al. 2018). This would help to understand whether the aversion of long-duration GRBs with bright optical afterglows to massive, luminous galaxies

is indeed a generic metallicity bias (Fruchter et al. 2006; Graham & Fruchter 2017), or largely a selection effect.

### 3.5. Fireball model tests

Afterglow emission from GRBs was predicted (Paczynski & Rhoads 1993; Katz 1994; Meszaros & Rees 1997; Sari & Piran 1997) prior to its discovery with BeppoSAX (Costa et al. 1997; van Paradijs et al. 1997). This afterglow emission is commonly described with the fireball model (Meszaros & Rees 1997). When the relativistically expanding blast wave interacts with the circumburst medium, an external shock is formed in which relativistic electrons gyrating in magnetic fields radiate synchrotron emission Wijers et al. (1997); Wijers & Galama (1999). Implicitly assuming that the electrons are “Fermi” accelerated at the relativistic shocks, and that they have a power-law distribution with an index  $p$ , their dynamics can be expressed with the following 4 parameters: (1) the total internal energy in the shocked region released in the explosion, (2) the density  $n$  (and its radial profile) of the surrounding medium, (3) the fraction of shock energy that goes into electrons,  $\epsilon_e$ , (4) ratio of the magnetic field energy density to the total thermal energy,  $\epsilon_B$ . This minimal and simplest afterglow model has only five parameters (not counting the distance/redshift).

The evolution of the afterglow emission in frequency space and with time depends on a number of additional boundary conditions, such as the properties of the burst environment (e.g., radial gas density profile, dust), on the progenitor (e.g., temporal energy injection profile), and details of the shock. Measuring the energetics (the fraction of energy going into the electrons  $\epsilon_e$  or into the magnetic field  $\epsilon_B$ ) or the energy partition ( $\epsilon_e/\epsilon_B$ ) has been challenging over the last 20 years. One particular difficulty is to distinguish between the fast or slow cooling stage which introduces an ambiguity in

the explanation of the spectrum in terms of the physical model parameters. The degeneracy between several of the above parameters makes it even more difficult to draw astrophysical conclusions from a given data set. Thus, many previous attempts in testing the fireball scenario had to make compromises, i.e. make assumptions about individual parameters (e.g., Panaitescu & Kumar 2002; Yost et al. 2003; Chandra et al. 2008; Cenko et al. 2010; Greiner et al. 2013; Laskar et al. 2014; Varela et al. 2016). Contradictions between results based on analyses with different assumptions surfaced only in the rare cases where the same GRB afterglows were analyzed using different data sets (e.g., McBreen et al. 2010; Cenko et al. 2011).

With its seven simultaneous channels, GROND provides an obvious advantage in these studies. Consequently, a number of attempts have been made to obtain data sets which would allow us to derive conclusions on the fireball parameters. The results are somewhat mixed, despite the fact that for most of these GRBs we achieved full wavelength coverage down to the sub-millimeter and radio bands. One of these unsatisfying examples is the bright afterglow of GRB 100621A. Three different emission components were identified, each with different spectral slope and temporal evolution, making a solution of even the simplest fireball scenario impossible (Greiner et al. 2013).

In a number of cases, the data collected with GROND (in conjunction with *Swift*/XRT and the long-wavelength coverage from the sub-mm to the radio) demonstrate convincingly that the most simplistic fireball scenario does not describe the data well, and thus extensions are required. GRB 091127 (Filgas et al. 2011b) was likely the first GRB afterglow with clear evidence for a moving cooling break, as expected in the fireball model, and even a measurement of the sharpness of the cooling break. However, the temporal evolution of the cooling break was

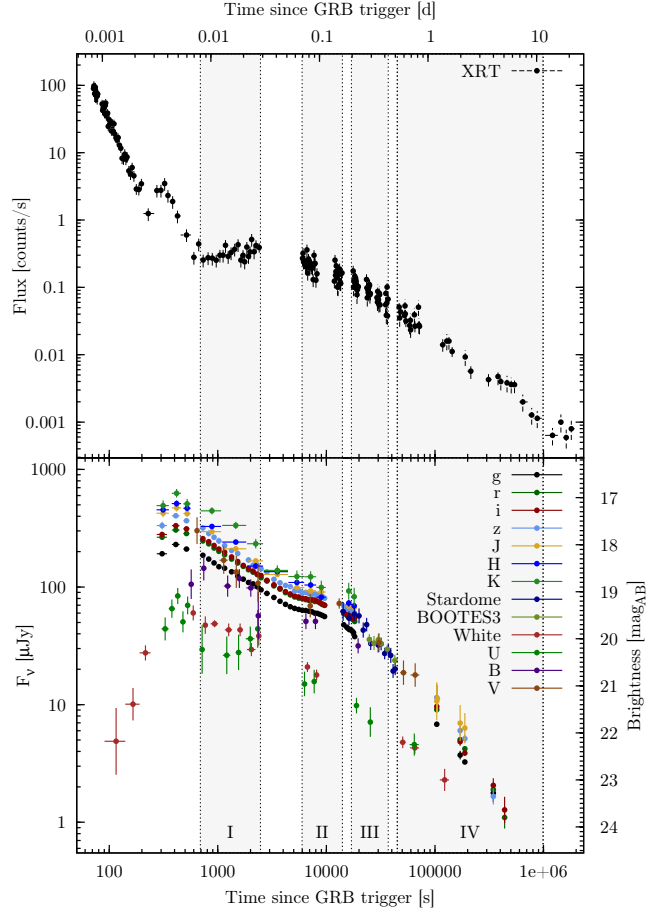


**Figure 6.** Light curve of the X-ray (top panel) and UV-to-NIR (bottom panel) afterglow of GRB 091029. Grey regions show the time intervals for which broad-band SEDs were formed. The nearly complete decoupling of the light curves in the two panels is difficult to reconcile with the fireball scenario. [From Filgas et al. (2012)].

clearly inconsistent with the standard fireball scenario. As one possible explanation of the data set, a temporal dependence of  $\epsilon_B$  was proposed (Filgas et al. 2011b), though a theoretical motivation remains to be given. The case of GRB 091029 may be extreme, with completely decoupled optical/X-ray behaviour (Fig. 6). A non-standard assumption for at least three fireball parameters was necessary, i.e. only a 2-component model with separate evolutionary states of each component could potentially explain the data set (Filgas et al. 2012). In several other GRB afterglows, the slopes of the elec-



tron distribution  $p$  as derived from the spectral slopes are clearly  $<2$ , as opposed to the canonical  $p = 2.2 - 2.3$ , thus leaving the particle acceleration mechanism and the high-energy cut-off(s) unsolved. Obviously, such results are unsatisfactory, and fresh ideas are needed to understand these events.

On a more positive note, GRB 121024A (Varela et al. 2016) shows a multi-colour light curve which is similar in X-rays and the optical/NIR band, and has additional sub-mm and radio data. This provided a showcase for an explanation within the basic fireball scenario. The ‘grain of salt’ was that some of the fireball parameters had rather extreme values, outside the range normally anticipated (though we might be misled by our expectations). So far the best, though still not perfect, case was GRB 151027B. Combining the X-ray and optical/NIR measurements with radio and ALMA data we could solve the fireball system, except for one parameter-pair ambiguity. Adopting the lowest-allowed total energy, all fireball parameters are well constrained, to at least a factor of three. The surprisingly and yet unexplained strong variability of the radio emission meant that those data were unusable in the fireball analysis (Greiner et al. 2018). This prevented a full-fledged test of the basic fireball scenario, including its temporal evolution. Interestingly, GRB 160625B also shows such strong radio variability (Alexander et al. 2017), suggesting that care must be exercised when using sparse radio data in GRB fireball modelling.

### 3.6. From prompt to afterglow emission: flares, bumps and jumps

One of the main motivations for building GROND was the fact that both the observed early-time rise/decay as well as non-powerlaw ‘bumps’ (e.g. in GRB 021004; Lazzati et al. 2002) exhibit variations faster than the time it takes to cycle through a number of filters. Only systematic observations in different filters as

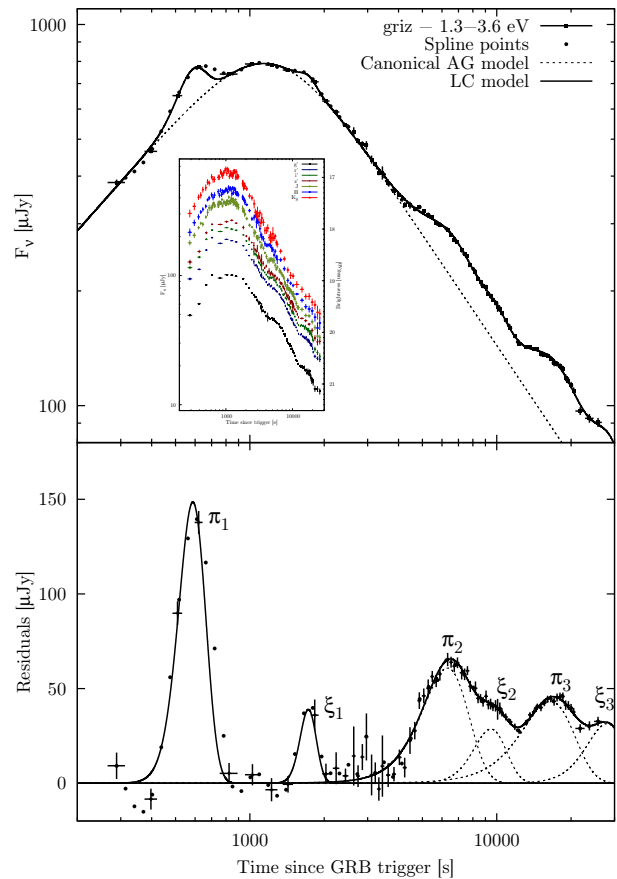


**Figure 7.** White light curve (upper panel) of the afterglow of GRB 071031, with the inset showing the complete 547 GROND  $g'r'i'z'JHK_s$  data points. The data were fitted using the sum of a smoothly connected power law for the canonical afterglow (dashed line) and Gaussian profiles to account for the evident flux excesses (solid line). The lower panel shows the residuals to the smoothly connected power law, and the six Gaussian models. [From Krühler et al. (2009a)]. ©AAS. Reproduced with permission.

synchronous as possible can overcome the ambiguity between effects of a changing spectrum or a highly variable achromatic emission.

Previously, four different mechanisms have been proposed to reproduce bumps or flares in optical afterglow light curves: (i) a superimposed reverse shock component for early flares, (ii) inhomogeneities in the circumburst medium (e.g., Wang & Loeb 2000), or (iii) the angular distribution of the energy in the jet (patchy shell

model; e.g., Kumar & Piran 2000), or (iv) late energy injection by refreshed shocks (e.g., Rees & Meszaros 1998) for later flares. However, a clear discrimination in the few individual, previously studied cases was not possible due to the lack of broad-band spectral information.

A first exciting case to demonstrate the advantage of the GROND seven-band imaging was GRB 071031: Superimposed onto the canonical afterglow emission, we found bumps which have a harder SED and appear to be simultaneous in the optical/NIR and at X-rays. Although emission from external shocks or a combination of different other effects cannot be ruled out, an internal origin seems to nicely account for the majority of observations (Krühler et al. 2009a): this includes the shape of the light curve and superposed bumps (Fig. 7), the spectral hardening towards the optical wavelengths, the observed temporal decrease of the peak energy  $E_{peak}$  between prompt emission and the flares, and the overall broadband flare spectrum from NIR to X-rays. The spectral similarities of the X-ray flares with the prompt phase suggest that they are later and softer examples of the prompt emission flares, and due to internal shocks. Thus, the simultaneous broad-band observation of GRB 071031 provides additional evidence that inner engine activity may last (or be revived) over hours or days, at least for some bursts.

A much more extreme case was the early (first few hundred seconds) optical/NIR emission after GRB 080129 (Greiner et al. 2009b): prior to the rising afterglow emission (peaking later than 7000 s after the GRB) a strong and rapid flare was observed, with an amplitude of 3.5 mag, and with a mean duration of 150 s. This was one of the rare occasions where emission related to a GRB was bright enough in the NIR bands in each of the 10 s sub-integrations. This allowed us to resolve the flare into sub-structure (Fig. 8), the shorter having a full-width at half

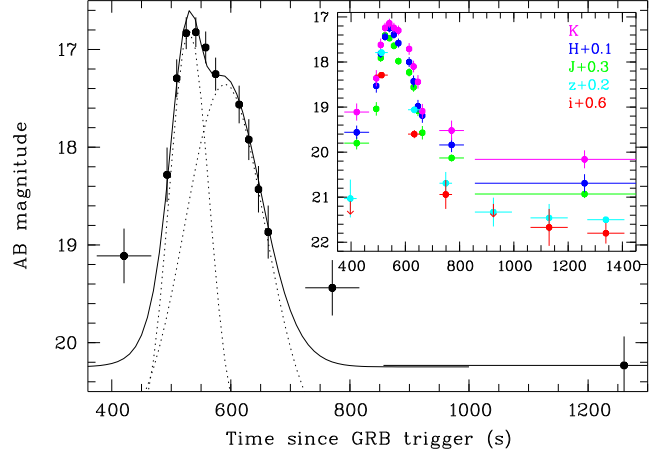


**Figure 8.** Co-added GROND  $JHK_s$  light curve (the inset shows the individual light curves plus those of  $i'z'$ ;  $g'r'$  are omitted due to Ly-absorption) of the early flare in GRB 081029. During most of the flare, the individual 10 s integrations are shown. The model (solid line) consists of the sum of two Gaussians (dotted lines) with FWHM of 77 and 157 s, respectively.

maximum (FWHM) of 77 sec. This is even more astonishing when considering the redshift of 4.3 for this GRB, i.e. the intrinsic rest-frame FWHM was 15 sec. The simultaneous observation in seven channels with GROND provides a SED from the optical to the near-infrared at a time resolution of once every minute. The delay of the flare relative to the prompt GRB, its SED as well as the ratio of pulse widths suggest that it arises from residual collisions in GRB outflows (Vlasis et al. 2011). Unfortunately, neither did *Swift*/XRT observe GRB 080129 at this time (blocked by Earth), nor did we ever detect a similar flare in another GRB in the following 8 years.

However, we did detect sudden intensity jumps in several GRBs at later times, between  $10^3$ – $10^4$  s after the GRB, with amplitudes in the 1-3 mag range. In these cases, the rise times were always much faster than the decay times. The “pulse” shapes ranged from triangular to nearly rectangular, thus justifying the term “jump” component, see e.g. GRBs

100621A (Greiner et al. 2013), 081029 (Nardini et al. 2011) or 100814A (Nardini et al. 2014). With a similar SED and only little simultaneous emission at X-rays (consistent with the slope of the optical/NIR SED slope), the same interpretation via residual collisions has been proposed.

### 3.7. GRB jet structure and off-axis appearance

Narrow jets, of order 5-20° opening angle, are usually invoked for the interpretation of the observed GRB emission primarily to reduce the otherwise huge inferred intrinsic energy budget. The opening angle of these jets as well as their radial energy distribution are then the next level of detail which need to be determined in order to constrain the GRB energetics.

It is usually assumed that all GRBs have the same universal (with some dispersion of the parameters) structure, but that they appear different because we see them under different observer angles  $\theta_o$  (Lipunov et al. 2001). The jet structure is assumed to be axisymmetric, and is defined by the radial distribution of the energy per jet unit solid angle  $\epsilon(\theta)$ , and that of the Lorentz factor  $\Gamma(\theta)$  of the emitting material. In models for an inhomogeneous or a structured jet ( $\epsilon(\theta) \propto \theta^{-s}$ ,  $s > 1$ ), the initial bulk Lorentz factor, the specific deceleration time and the radius are dependent on the distance from the symmetry axis of the jet (Rhoads 1999; Granot & Kumar 2003). Thus, a geometric offset of the observers from the jet symmetry axis has a distinct signature in the observed optical light curve. Because of the relativistic beaming of the decelerating ejecta, an observer located off-axis will see a rising optical afterglow light curve at early times (e.g. Panaitescu et al. 1998; Granot et al. 2002), with the steepness of the rise being characteristic of the off-axis angle and the jet structure. For the interpretation of afterglow light curves the structured jet is often approximated by a two-component jet, i.e. narrow jet

with high  $\Gamma$  surrounded by a wider cone with small  $\Gamma$ .

For two bright GRB afterglows, GROND data argue for a two-component jet structure as preferred interpretation. The multi-band afterglow light curve of GRB 080710 (Fig. 9) shows two salient features, both achromatic to high precision: an early rise in its brightness, too shallow to be caused by a jet in the pre-deceleration phase, and a turnover from a shallow to a steep decline without a change in spectral slope, thus incompatible with a jet break (Krühler et al. 2009b). The most natural explanation is a two-component jet (Fig. 9), with the narrow component (2°-4° opening angle) viewed slightly off-axis, and the wider component with lower Lorentz factor dominating the late emission. In this interpretation, the shallow decay phase is the result of the superposition of the narrow-jet afterglow and the rise of the broad jet in its pre-deceleration phase (Krühler et al. 2009b).

GRB 080413B is well fit with an on-axis two-component jet model. The narrow ultra-relativistic jet is responsible for the initial decay, and the rising of the moderately relativistic wider jet causes a re-brightening and dominates the late evolution of the afterglow (Filgas et al. 2011a). The deduced jet opening angles are 2° and 9° respectively, for the narrow and wide jet, and the initial Lorentz factors  $> 190$  and  $19$ . This model also explains the relative fluxes and spectral shapes of the X-ray vs. optical/NIR emission as well as the chromatic re-brightening due to the different spectral regime of the wide jet.

In both cases, the early and very accurate multi-colour light curves provided by GROND were essential in excluding alternative explanations, such as a reverse shock, emission during the pre-deceleration phase, refreshed shock emission, or an inhomogeneous ISM density profile (Krühler et al. 2009b; Filgas et al. 2011a).

### 3.8. Short-duration GRBs

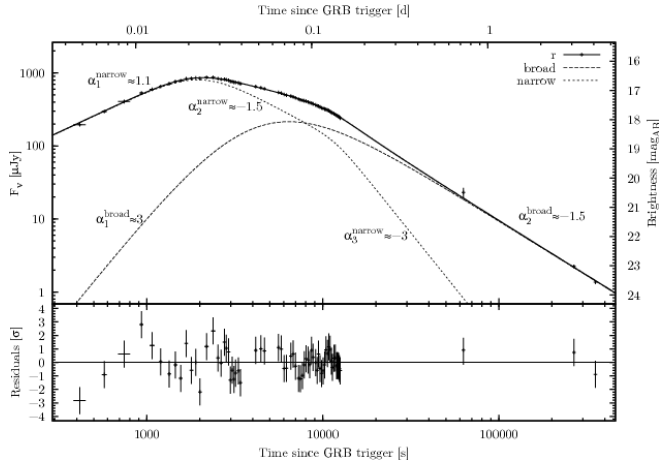


**Figure 9.** GROND  $r'$  light curve of the afterglow of GRB 080710 (upper panel) with the best fit (solid line) of a two-component jet model with  $\nu_m < \nu_{opt} < \nu_X < \nu_c$  for both components. The narrow jet (dotted line) is seen off-axis and produces a shallow rise as its emission spreads during deceleration. The broad jet (dashed line) is viewed close to on-axis with initial Lorentz factor  $\sim 50$  and opening angle  $> 10^\circ$ , and has the expected step rise during its pre-deceleration phase. [From Krühler et al. (2009b)].

Since the afterglows of short-duration GRBs are substantially less luminous, their discovery was accomplished only in 2005 (Fox et al. 2005) with the advent of the fast and accurate localization with the Gehrels *Swift* Observatory (Gehrels et al. 2004). The faint optical afterglows also meant that small robotic telescopes had little success and impact. Even with GROND at a 2m class telescope, the detection rate of short GRBs is a factor of two smaller than that for long GRBs (see Fig. 3), and the detections typically do not extend beyond 2–3 days after the GRB. Yet, this was long enough for GROND to establish the first cases of clear jet-breaks in the afterglows of short-duration GRBs (Nicuesa Guelbenzu et al. 2011, 2012). This provided first observational hints that the jet opening angles in short GRBs are wider than those in long-duration GRBs, as earlier suggested on theoretical grounds (Aloy et al. 2005).

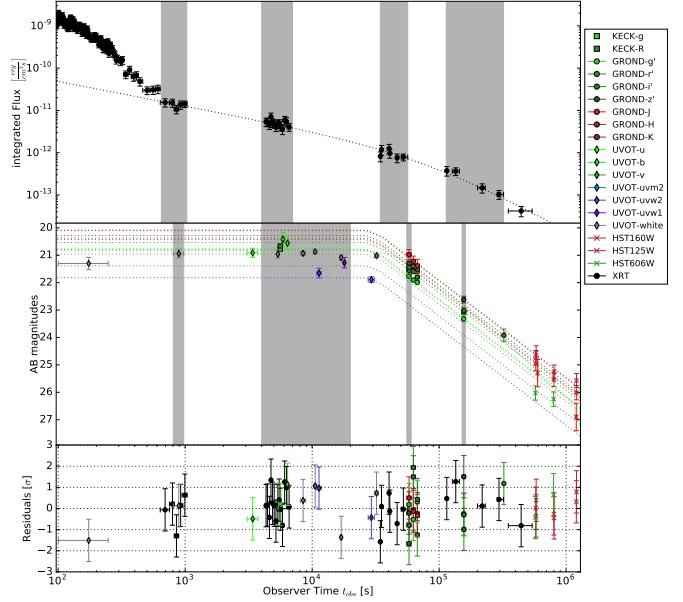


**Figure 10.** X-ray and optical light curve of the afterglow of the short-duration GRB 150424A. The grey-shaded areas indicate the time slices used for the SED analysis which together with the best-fit temporal slopes allows us to reject all standard scenarios. [From Knust et al. (2017)].

Apart from their duration and peak energy, short GRBs show many phenomenological properties similar to long GRBs. Among those properties is optical plateau emission, e.g. GRB 060313A (Roming et al. 2006), GRB 061201A (Stratta et al. 2007), or GRB 130603B (Fan et al. 2013). A particularly well-sampled example is GRB 150424A (Fig. 10), where our GROND data provide convincing evidence for a uniform, nonspreading jet expanding into an ISM medium as a self-consistent explanation (Knust et al. 2017), where the jet is re-powered for  $10^4$  s with additional constant energy injection. Within a factor of two, this unique and very-long-duration energy injection in GRB 150324A provides a similar energy input as the prompt GRB emission (Knust et al. 2017).

### 3.9. GRB hyper- and kilo-novae

The association of hydrogen- and helium-free core-collapse supernovae (type Ic) to long-



duration GRBs, first seen in GRB 980425 / SN 1998bw (Galama et al. 1998) and then conclusively observed for GRB 030329 / SN 2003dh (Hjorth et al. 2003; Stanek et al. 2003) has established their relation to exploding massive stars. The kinetic energy of both supernovae was in excess of  $10^{52}$  erg, a factor 10 larger than canonical SNIc, and thus earning the name ‘hypernovae’ (though that name has been in use already since the early 80ies). The inferred rates of SNIc and GRBs differ by at least a factor of 100 (depending on the actual GRB beaming angle), and the still debated question is what causes a small fraction of supernovae to produce a GRB (Woosley et al. 1999)?

Despite having now over 700 GRBs with an observed optical afterglow, less than 50 GRB-supernovae are known to varying degree of confidence, and only 11 of these have strong spectroscopic evidence in the optical (Cano et al. 2017). Partially, this is due to the fact that the supernova light is getting difficult to observe beyond redshift  $z \sim 0.5$ , but certainly also the lack of systematic late-time ( $\sim 10$  days) optical monitoring implies that many GRB-supernovae are missed. With our concept of following each observable GRB as long as ‘something’ is detected, GROND observations at least doubled the annual rate of discovered GRB-supernovae (e.g. Cano et al. 2014; Olivares et al. 2012, 2015; Kloze et al. 2018).

GRB 111209A / SN 2011kl turned out to be particularly interesting, as the prompt emission had an ultra-long duration ( $>4$  hrs), revealed with the Konus detector on the WIND spacecraft (Golenetskii et al. 2011). The GRB occurred at a redshift of  $z = 0.677$  (Levan et al. 2014), as determined from afterglow spectroscopy. Its integrated equivalent isotropic energy output is  $(5.7 \pm 0.7) \times 10^{53}$  erg (Golenetskii et al. 2011), corresponding to the bright end of the distribution of long-duration GRBs. Several models had been proposed to explain the

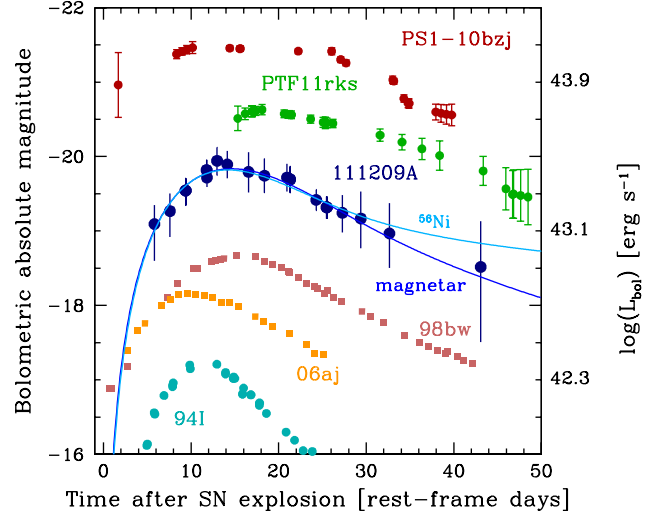


**Figure 11.** Afterglow- and host-subtracted bolometric light curve of the supernova related to GRB 111209A as observed with GROND ( $g'r'i'z'J$ ) in the 2300–8000 Å rest frame, compared with bolometric light curves of GRB 980425 / SN 1998bw (Galama et al. 1998), XRF 060218 / SN 2006aj (Pian et al. 2006), the standard type Ic SN 1994I (Sauer et al. 2006), and the superluminous supernovae PTF11rks (Inserra 2013) and PS1-10bjz (Lunnan et al. 2013). The dark blue line shows the best-fitting synthetic light curve computed with a magnetar injection model based on Kasen & Bildsten (2010). The bright blue line shows the best-fit  $^{56}\text{Ni}$  light curve. [From Greiner et al. (2015)].

ultra-long duration of GRB 111209A (and a few others), but the otherwise inconspicuous spectral and timing properties of both, the prompt and afterglow emission as well as the GRB host galaxy properties, provided no obvious clues to distinguish among these (Gendre et al. 2013; Levan et al. 2014; Nakauchi et al. 2013).

The corresponding GRB-supernova SN 2011kl was a factor of  $>3x$  more luminous and its spectrum distinctly different from other type Ic supernovae associated with long-duration GRBs. The slope of the optical continuum resembles those of super-luminous supernovae, but the light curve evolved much faster (Fig. 11). The combination of high bolometric luminosity but low metal-line opacity cannot be reconciled with

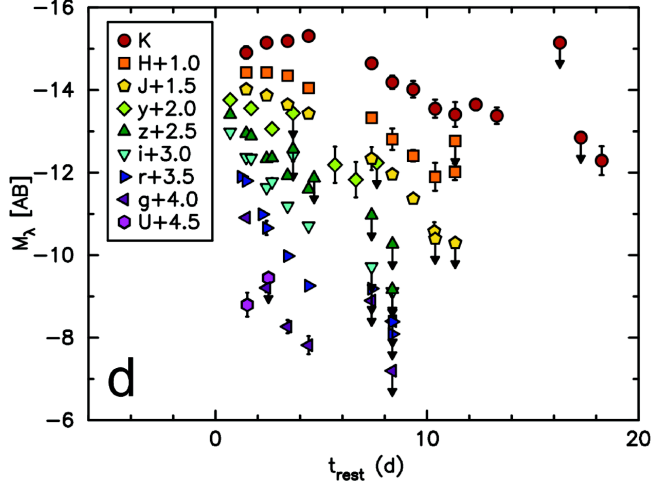


**Figure 12.** GROND lightcurve of the kilonova of GRB 170817A, with selected  $U$ –, and  $K$ –band (NTT) as well as  $y$ –band (PS1) data points, corrected for Galactic foreground extinction and transformed to absolute AB magnitudes using the distance of 40 Mpc. [From Smartt et al. (2017)].

typical SN Ic, like in all previous GRB-SNe. Instead, it can be reproduced by invoking a magnetar, a strongly magnetized neutron star, which injects extra energy (Greiner et al. 2015; Kann et al. 2018). The detection of a supernova associated with the ultra-long GRB 111209A immediately rules out a tidal disruption event as the origin of GRB 111209A (Levan et al. 2014). Also, blue supergiants (Nakauchi et al. 2013) are ruled out as progenitors, since they show hydrogen in their spectra and have substantially different light curves (Kleiser et al. 2011), inconsistent with our observations. Instead, GRB 111209A / SN 2011kl provides a link between GRB/SNe on the one hand, and ultra-long GRBs and superluminous SNe on the other.

The short-duration burst GRB 170817A became famous for its gravitational wave detection (Abbott et al. 2017a). It occurred extraordinarily nearby at 40 Mpc, or  $z = 0.009$  (Abbott et al. 2017b; Burgess et al. 2017), thus its kilonova was in reach for even small telescopes. Yet, the short visibility period per night ( $\sim 1$  hr) made

GROND’s simultaneous 7-channels again particularly useful (Fig. 12). As the kilonova faded, the SED rapidly changed from blue to red, and a higher-opacity, lanthanide-rich ejecta may have contributed to the late-time emission. The decline is measured to have a power-law slope of  $1.2 \pm 0.3$  (Smartt et al. 2017) which is consistent with radioactive powering from  $r$ -process nuclides. The derived physical parameters broadly match the theoretical predictions of kilonovae from neutron-star mergers (e.g. Metzger et al. 2010; Kasen et al. 2013).

## 4. IDENTIFICATION OF TRANSIENT OR STEADY HIGH-ENERGY SOURCES

### 4.1. X-/ $\gamma$ -ray Transients

Most objects which presently trigger high-energy missions with their X-ray or  $\gamma$ -ray transient behavior (Kennea 2015; Abdollahi et al. 2017; Negoro 2017) are accreting systems, exhibiting either thermal emission from accretion disks, bremsstrahlung due to shocks in winds, or synchrotron emission in jets. Consequently, enhanced emission at other wavelengths is accompanying the X-/ $\gamma$ -ray transients, often at optical and/or near-infrared wavelengths, originating predominantly either in the accretion disk or the jet. Galactic sources do occur mostly in the disk of the Milky Way, making near-infrared observations more promising due to the smaller affect of absorption by dust.

With varying degree of effort over the years, newly discovered X-ray transients from *Swift*, MAXI or the XMM-*Newton* slew survey were followed up with GROND. Typically, results were published within hours (e.g. 32 Astronomical Telegrams between 2008-2016), with about 50% of these reporting discoveries of the optical/NIR counterpart.

These identifications predominantly rely on the detection of a new or substantially brightened source relative to a reference catalog. The 7 simultaneous GROND channels and the cor-

responding spectral energy distribution are particularly useful in assigning source classes even for non-variable objects. As Fig. 13 shows, accreting sources (blue SEDs) can be easily distinguished from blazars or GRB afterglows (red SEDs), or stellar objects. One example was INTEGRAL trigger 5994, which reported a discovery of a long-duration GRB (Mereghetti et al. 2010), but was shown to be a variable object with a stellar SED; this allowed us to reject the GRB classification (Updike et al. 2010).

#### 4.2. Tidal disruption events

Tidal disruption events (TDEs) are obviously another very intriguing type of transient which were followed-up with GROND at various occasions (e.g. Cappelluti et al. 2009; Komossa et al. 2009; Merloni et al. 2015). TDEs ensue when a star gets close to a supermassive black hole (SMBH) in the center of a galaxy, and is ripped apart by the tidal forces of the black hole.

TDEs promise to help solving several astrophysical questions, among others about the accretion formation and physics in early stages of TDE evolution (Lodato et al. 2015), the formation and ejection of relativistic jets, the prevalence of (dormant) single or binary SMBHs in

galaxies (Komossa 2017), or verifying signatures of General Relativity (delay in accretion disk formation or quasi-periodic modulations at X-rays; Stone et al. 2018).

Observations of Swift J2058.4+0516, the possible second relativistic TDE discovered, revealed faint optical emission despite small intrinsic extinction, suggesting that either the outflows are extremely narrowly collimated, or that only a small fraction of tidal disruptions generate relativistic ejecta (Cenko et al. 2012).

The unusual transient OGLE16aaa, recently detected by the Optical Gravitational Lensing Experiment (OGLE-IV) survey (Wyrzykowski et al. 2016; Greiner et al. 2016), shows many optical features similar to other TDEs. The spectral properties and photometric history of the host galaxy suggest that OGLE16aaa belongs to a sub-class of TDEs which is associated to weakly or only recently active SMBHs. This class might provide a connection between TDEs from quiescent SMBHs and flares observed as ‘changing-look quasars’, if the latter are interpreted as TDEs. In this case, the previously applied selection criterion for identifying a flare as a TDE to have come from an inactive nucleus, would represent an observational bias, thus affecting TDE-rate estimates (Wyrzykowski et al. 2017).

#### 4.3. Steady sources

The characterization and typography of sources via the 7-channel SEDs can obviously be used also for steady sources, i.e. for the optical/NIR identification of X-/ $\gamma$ -ray sources. Applications of this possibility have not yet been published, but observations have been taken for unidentified ROSAT sources; a wider use is anticipated for new X-ray sources which the upcoming eROSITA survey will discover.

Identifying individual galaxies as belonging to the same galaxy cluster by color selection is a wide-spread method. Using GROND with its seven simultaneous channels allows not only for

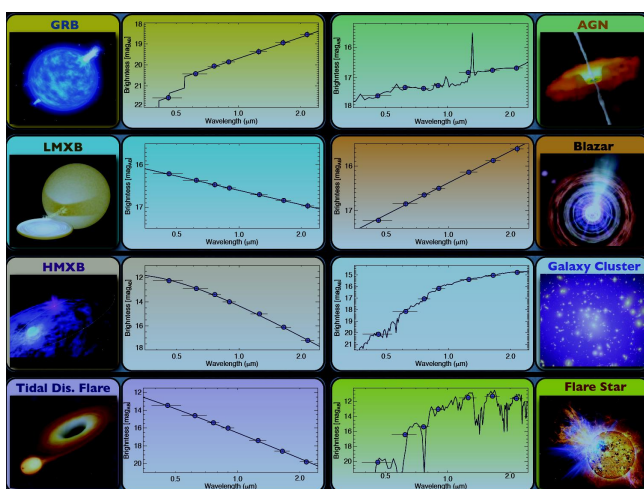


**Figure 13.** Source typing power of GROND via its simultaneous 7-channel imaging capability [From Rau (2012)].

a substantially more secure selection (by using the full SED instead of the usual two filters), but also a photometric redshift estimate of individual cluster members (see e.g. Pierini et al. 2012 for a cluster at  $z=1.1$ ).

A more unusual application of this method was the search for a suspected companion star of a neutron star formed in a supernova which created the remnant RCW 86. GROND observations identified such a candidate with uncommon SED-shape which allowed to justify follow-up VLT spectroscopy. This in turn revealed that this neutron star companion was strongly polluted with calcium and other elements. Combining all constraints suggests that the progenitor of the supernova that produced RCW 86 was a moving star which exploded near the edge of its wind bubble and lost most of its initial mass because of common-envelope evolution shortly before core collapse (Gvaramadze et al. 2017).

## 5. X/ $\gamma$ -RAY BINARIES

### 5.1. Heating in a $\gamma$ -ray pulsar

Color variations over orbital phase in X-ray or  $\gamma$ -ray binaries are frequently observed. Simultaneous multi-color observations such as with GROND are particularly rewarding for short orbital periods. One interesting example is the  $\gamma$ -ray black widow pulsar PSR J1311-3430 (Romani et al. 2012). Black widow pulsars are binaries consisting of a millisecond pulsar and a very low-mass star (brown dwarf), in which the strong radiation from the neutron star ablates the companion, thus leading to outflows strong enough to eclipse the pulsar signal for a good fraction of the orbit. Black widow systems allow an accurate neutron star mass determination, and consequently constraints on the equation of state of neutron stars (Lattimer & Prakash 2011).

The bright  $\gamma$ -ray source 2FGL J1311.7-3429 (3FGL J1311.8-3430), known since the early

EGRET mission (3EG J1314-3431), was identified as a 2.5 ms pulsar in Fermi-LAT data once an optical counterpart had been found. With an orbital period of 94 min, it shows more than 3 mag amplitude variations. Spectroscopy revealed that the companion is a bloated, Roche-lobe filling substellar object with a He-dominated photosphere, while no hydrogen is seen. GROND photometry showed a strong color variation with orbital period (Fig. 14), and a reddening at the pulsar’s superior conjunction by  $g'-r' \sim 0.6$  mag. At maximum light, the colors in the visible wavelength range are comparable to those of a B8 star, while in the NIR there is a large excess. This suggests a large emitting area at low temperature. One possible source is the evaporative wind, reprocessing the pulsar power into the optical/NIR. Also, short-term variability (flares) are very red, suggesting a variable wind off the companion.

The flat part of maximum light is a challenge to light curve fits: neither cold nor hot asymmetric spots helped to improve the fits, suggesting additional physics to be at play. As these additional model components also affect the best-fit inclination, the neutron star mass estimate remains rather poor: depending on the exact modelling of the near-infrared flux, we obtained 2.2-2.8  $M_{\odot}$  (Romani et al. 2012). Later, more detailed phase-resolved spectroscopy and more sophisticated light curve models also allow a mass as low as 1.8  $M_{\odot}$  (Romani et al. 2015). Yet, the neutron star mass determined for this black widow remains interestingly high.

The *Fermi* satellite has proven to be efficient in finding black widows with short orbital periods, with another 100 candidates waiting for careful analysis. In an exploratory search for another dozen candidates, only one more clear example could be identified via few-hour GROND light curves (e.g. Salvetti et al. 2015, 2017).

### 5.2. The closest jet source?



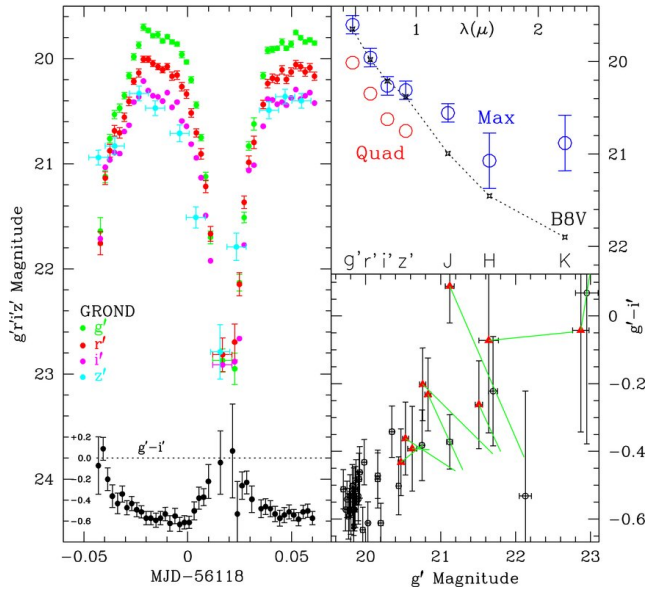


**Figure 14.** GROND  $g'r'i'z'$  light curve (left) with the  $g'-i'$  color change at the bottom, showing reddening during the minimum, the pulsar superior conjunction. The upper right panel shows the large NIR excess of the SED in comparison to a B8V star. The lower right shows the color variations with brightness, where green lines and red triangles mark epochs with  $\Delta g' > 0.2$  mag over the quiescent magnitude. From Romani et al. (2012). ©AAS. Reproduced with permission.

During the search for the counterpart of a serendipitous Chandra X-ray source with an X-ray jet (CXO J172337.5-373442), a candidate in the optical/NIR was identified with GROND observations. Consistent values of visual extinction (as determined from the GROND SED) and hydrogen column density (as determined from the X-ray spectrum) as well as the spatial coincidence suggest that the optical source is associated with the X-ray source. The good match of an extrapolation of the GROND NIR fluxes to that of a nearby Spitzer source suggests an association as well, with the full SED being consistent with a G9 V star at a distance of  $330 \pm 60$  pc. Since the observed X-ray luminosity cannot be explained in terms of emission from a single G9 star, it is likely that CXO J172337.5-373442 is an accreting compact object in a binary sys-

tem (Mookerjee et al. 2010). This makes it the nearest known resolved X-ray jet from a binary system which is not a symbiotic binary. The implied very low X-ray luminosity of only  $7 \times 10^{30}$  erg s $^{-1}$  (assuming isotropic emission) is at odds with the standard concept of jet ejection in 'high-states' of the accretion disk. Even if this system is a cataclysmic variable, the jet was launched in a state of quiescence. This implies that such jets are more ubiquitous than previously thought, because they are difficult to detect at much larger distances (Mookerjee et al. 2010).

## 6. BROWN DWARFS

### 6.1. *Ross 458C: A benchmark T8-9 brown dwarf*

More than half of all stars (brown dwarfs included) have masses below  $0.2 M_{\odot}$ . The formation mechanism of these stars is uncertain, with theory suggesting turbulent fragmentation, ejection of protostellar embryos, disc fragmentation or photo-erosion of prestellar cores (Stamatellos 2017). Brown dwarfs are objects below the hydrogen burning limit (mass range of  $0.01$ – $0.75 M_{\odot}$ ). The oldest brown dwarfs could be as old as the first generation of stars that formed in the Universe. Brown dwarf studies have gained momentum with the discovery of objects with decreasingly lower temperature and the growing evidence that brown dwarfs and giant gas planets overlap in masses and global temperature (Chabrier et al. 2014).

Benchmark brown dwarfs are systems with well-known properties such as effective temperature, parallax, age and metallicity. GROND follow-up of candidates from a search of the DR5+ release of the UKIRT Deep Infrared Sky Survey revealed an object which shared its large proper motion with an active M0.5 binary at 102 arcsec distance, forming an hierarchical low-mass star and brown dwarf system (Goldman et al. 2010). With a mass of only 14 Jupiter

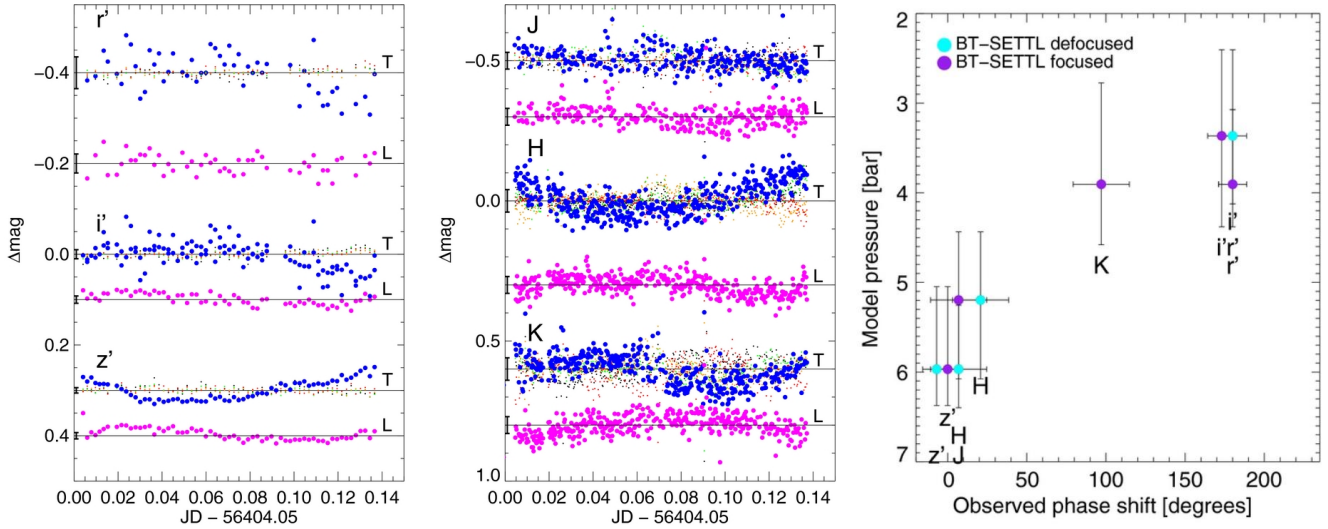


**Figure 15. Left and Middle:** GROND light curves of the L7.5 (red) and T0.5 (blue) component, respectively. Error bars are plotted at the very beginning of each light curve, and a (normalized) example residual light curve is shown in grey small dots. **Right:** The atmospheric pressure dependence on phase shift based on the one-dimensional model of Allard et al. (2012) [From Biller et al. (2013)]. ©AAS. Reproduced with permission.

masses and a distance of 11.4 pc, this young (less than 1 Gyr) system is a promising target to constrain the evolutionary and atmospheric models of very low-mass brown dwarfs (Goldman et al. 2010; Burningham et al. 2011).

### 6.2. Weather on the nearest brown dwarf

Luhman16AB or WISE J104915.57-531906.1AB is the closest ( $2.0 \pm 0.15$  pc) brown dwarf pair ( $1''.5$  or 3 AU separation) with an L7.5 primary and a T0.5 secondary (Luhman 2013) and thus a prime target to search for dusty cloud structure break-up (Biller et al. 2013, and references therein). Two sets of 4-hr observations each with GROND in April 2013, revealed anti-correlated variability between different filters (Fig. 15), as well as a phase offset of the  $K$  band light curve relative to  $H$  and  $z'$  (Biller et al. 2013). This offset is correlated with atmospheric pressure, as it can be probed in each filter band (right-most panel of Fig. 15), as estimated from one-dimensional atmospheric models. Follow-up CRIRES/VLT observations clearly show spectroscopic variability over the rotation phase, and Doppler imaging makes

this patchy global cloud structure visible in the stellar surface map of the B component of the system (Crossfield et al. 2014).

### 6.3. New identification: J021003.48-042512.7

The spectral energy distributions of brown dwarfs are similar to those of quasars at redshifts around 6, and thus are a frequent contaminant of color-color search algorithms for high- $z$  QSOs. Since GRB afterglows were usually observed until they were not detectable anymore in a 1-2 hr exposure, stacking of the individual exposures give deep images around the GRBs observed since 2007. During the search for high- $z$  QSOs in these deep GRB fields, one particularly interesting example was J021003.48-042512.7 ( $\pm 0''.5$ ) which has been found in a stack of 160 min GROND exposure of GRB 131011A (Fig. 16). With AB magnitudes of  $z' = 23.3 \pm 0.1$ ,  $J = 20.9 \pm 0.1$ ,  $H = 21.1 \pm 0.1$ ,  $K = 21.2 \pm 0.3$  mag, it is close to T dwarfs or  $z \sim 7$  QSOs in color-color space. We thus obtained a short (10 min exposure) VLT/X-shooter spectrum on 13 Feb. 2014 which clearly solved the ambiguity (Fig. 17): a NIR spectral type of

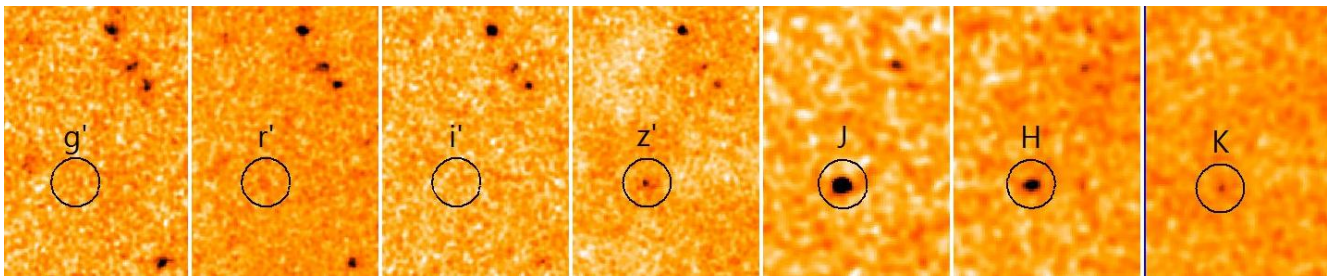


**Figure 16.** GROND 7-channel finding chart of the brown dwarf J021003.48-042512.7; North is at the top, and East to the left. The image sizes are  $23'' \times 33''$ .

$T5 \pm 1$  provides the best match for this brown dwarf using the templates of [Burgasser et al. \(2006\)](#). Using  $M_H = 14.8$  mag (Vega) from [Kirkpatrick et al. \(2011\)](#), the distance of the brown dwarf J021003.48-042512.7 is  $100 \pm 30$  pc. Being about 3 mag fainter than the WISE limit, this is one of the most distant T dwarfs known.

## 7. EXOPLANETS

More than 20 years after the discovery of the first planet outside our solar system, more than 2000 exoplanets with very diverse properties have been discovered. With this large population, the field has moved from discovery to characterization. Obviously, the largest interest lies in the study of the atmospheric conditions, including their temperatures, albedos, compositions and cloud structures. But for the

basic geometric properties like orbital periods and masses, transit measurements are one of the most important methods ([Cameron 2016](#)).

Exoplanet transit observations benefit from simultaneous multi-filter imaging in several ways. Firstly, it safely distinguishes proper transits from potential blends between a star with a faint eclipsing-binary system. This was nicely demonstrated by [Snellen et al. \(2009\)](#) for OGLE2-TR-L9 where the mother star turned out to be an early F-star ([Lendl et al. 2010](#)). Secondly, it allows to recognize flares or spots on the mother star which otherwise affect the interpretation of the light curve (e.g. [Mancini et al. 2013](#); [Mohler-Fischer et al. 2013](#)). Thirdly, it provides evidence for grazing eclipses, since the limb darkening predominantly affects the bluer wavelengths (see Fig. 18; [Mancini et al. 2014](#)). Furthermore, GROND's coverage of the NIR wavelengths enables the measurement of the vertical temperature profile via flux ratios to the mother star, since layers at different depth are simultaneously probed at different filter bands ([Chen et al. 2014](#)). Last but not least, differences in the ingress and egress slopes can be used to infer basic chemical ingredients of the planetary atmosphere. Overall, exoplanet studies are likely the science topic with the largest use of GROND observing time over the last decade.

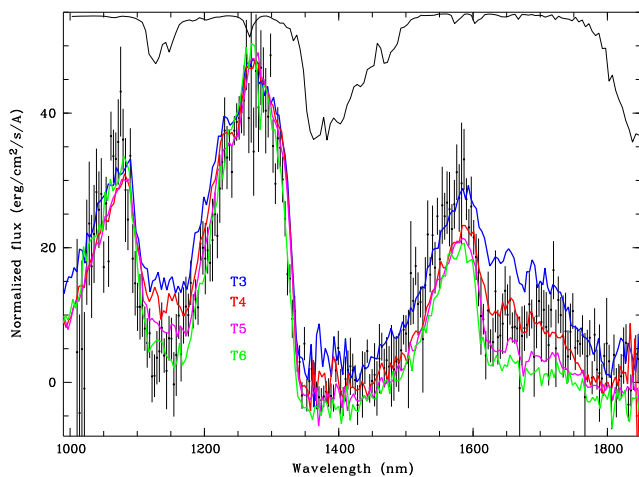


**Figure 17.** X-shooter spectrum of J021003.5-042512 with template spectra of selected T dwarfs overlotted.

## 8. BLAZARS: PHOTOMETRIC REDSHIFTS DOWN TO $Z \sim 1$

With the majority of GRBs occurring at redshift  $< 2$ , but the lowest-redshift GROND dropouts ( $g'$  dropout) measurable only at around  $z \sim 3$ , GROND alerts to the community for high-redshift GRBs was not particularly large, at the 20% rate. However, the sensitivity can be extended to lower redshifts by combining GROND observations with simultaneous observations at wavelengths bluer than GROND- $g'$ . For instance, the combination with Swift/UVOT (Fig. 19) allows photometric redshifts as low as  $z \sim 1.2$ . In this particular case, even non-simultaneous observations can be used, as the UVOT- $b$  filter closely matches the GROND- $g'$  filter, which thus can be used for the relative cross-calibration.

Examples for such application are GRB afterglows (Krühler et al. 2011a) and BL Lac objects (Rau et al. 2012; Kaur et al. 2017). In both cases, the intrinsic spectral energy distribution is a (sometimes broken) power law, and thus the Ly- $\alpha$  drop creates a clear signature, leading to typical photometric redshifts errors of  $\Delta z/(1+z) \sim 10\%$  for  $z > 1.5$  (Fig. 20). The dust-redshift degeneracy is broken with increasing redshift, as the Ly-limit moves to redder wavelengths, producing a drop-out at bluer filters which is too sharp to be mistaken by dust absorption. The redshift accuracy remains es-

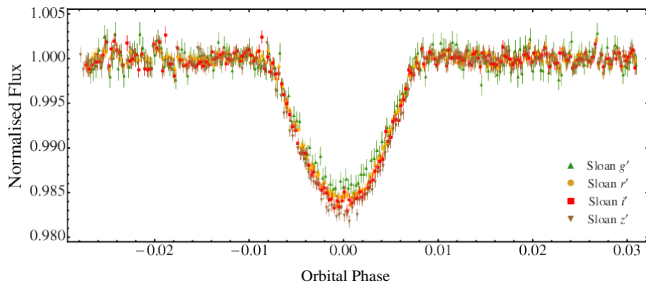


**Figure 18.** GROND  $g'r'i'z'$ -band light curves of one WASP-67b eclipse, showing its wavelength-dependence: the bluer the color, the shallower the transit, as expected for a grazing eclipse, as limb darkening is stronger at bluer wavelengths. [Adapted from Mancini et al. (2014)].

entially constant until  $z \sim 6.5$ , demonstrating that the total number of individual filters does not strongly affect the robustness of the photo- $z$  measurement, as long as the intrinsic continuum is fairly well known (as in GRBs and BL Lacs).

## 9. HIGH-REDSHIFT QUASARS

The search for high redshift ( $z \gtrsim 6$ ) has been an area of intense work over the last decade, given that early versions of their luminosity functions indicated rather high surface density. The majority of searches were based on the dropout technique, and the challenge for color selections is the high incident of low-redshift contaminating sources (e.g. brown dwarfs, redshift two galaxies). Down-selecting candidate lists in preparation of follow-up spectroscopy then is the area where imaging with GROND

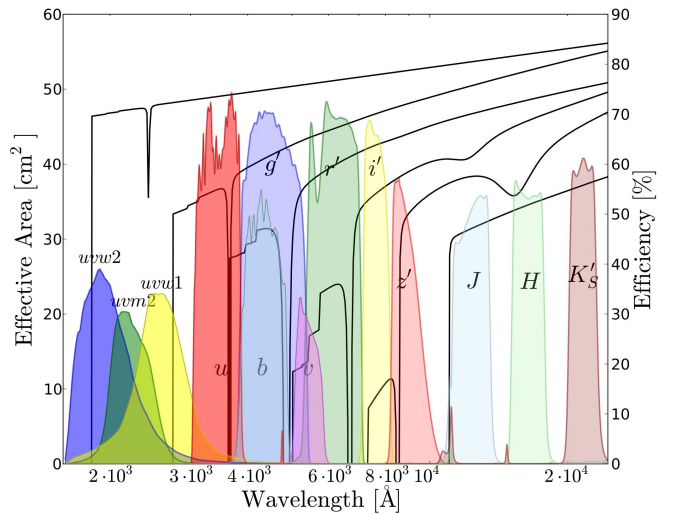


**Figure 19.** Swift/UVOT ( $uvw2$ ,  $uvm2$ ,  $uvw1$ ,  $u$ ,  $b$ ,  $v$ ) effective areas (left y-axis) and GROND ( $g'r'i'z'JHK_s$ ) filter transmission curves (right y-axis), respectively. The GROND filter curves include all optical components including the telescope. Shown with black solid lines are template afterglow spectra for redshifts  $z = 1, 2, 3, 4.5, 6$  to  $8$  (top left to bottom right). These spectra also differ in their spectral index and rest-frame extinction (both, amount and reddening law),  $2175 \text{ \AA}$  dust feature, and damped Ly- $\alpha$  absorption. [From Krühler et al. (2011a)].



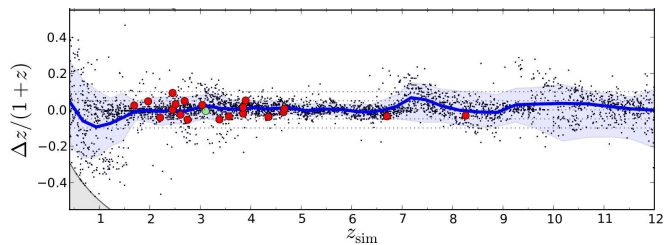


**Figure 20.** Simulated photometric redshift accuracy (grey dots) vs. observed GRBs with GROND+Swift/UVOT for which spectroscopic measurements are available (red dots). The green dot shows the photo- $z$  of the flat-spectrum radio quasar PKS 0537-286 derived in a similar manner ( $z = 3.10$ ; Bottacini et al. (2010)). The thick blue line shows the average photometric redshift after distributing the 4000 mock afterglows into redshift bins of 100 afterglows each, and the blue-shaded area shows the  $1\sigma$  statistical uncertainty. [From Krühler et al. (2011a)].

is most efficient. Indeed, GROND has played a major role in this task (Banados et al. 2014; Venemans et al. 2015; Banados et al. 2016; Mazzuchelli et al. 2017).

After achieving a sample size of a few dozen quasars at  $z > 6$ , several physically interesting new aspects arose. One of those, with direct impact on multi-colour imaging, is the unexpectedly large variance in the strength of the Ly- $\alpha$  (+ N V) emission line (see Fig. 21): for the 10% of quasars with the smallest Ly- $\alpha$  + N V equivalent width, the line is virtually absent, and thus they resemble weak-emission line objects (Banados et al. 2016). This is substantially more than at lower redshift. But whether this is an evolutionary effect or an observational bias (by the filter setting or the increase in the neutral hydrogen fraction, or both), remains to be investigated.

## 10. CONCLUSION

The design of the GROND instrument was originally developed for GRB afterglow observations. Nevertheless, many other science areas have greatly benefited from the simultaneous

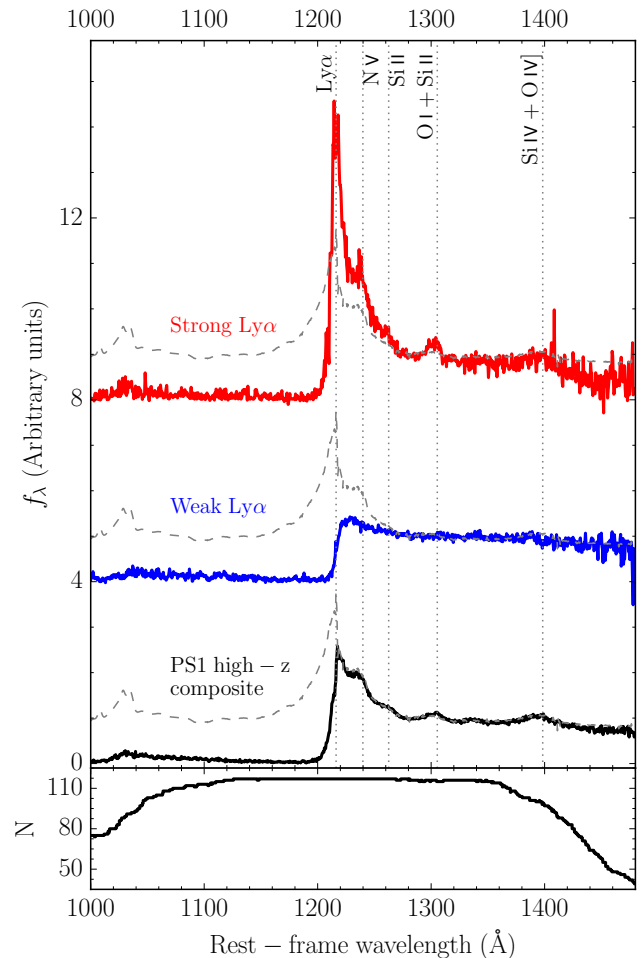


**Figure 21.** Top: Diversity of high- $z$  QSO emission spectra, showing those with the 10% strongest (red) and weakest (blue) Ly- $\alpha$  equivalent width, compared to the low-redshift composite (gray) of Selsing et al. (2016) and the arithmetic median of all 117 QSOs (black) of Banados et al. (2016). Bottom: number of QSOs per wavelength bin contributing to the median of 117 QSO spectra. [From Banados et al. (2016)].

7-channel imaging of GROND. GRB follow-up observations used only about 15% of the 2.2m telescope time between 2008–2016, yet provided noteworthy results for 112 refereed publications, and supported 12 PhD theses. The biggest impact of GROND observations of GRBs was undoubtedly the initiation of systematic afterglow follow-up in the near-infrared ( $JHK_s$ ), enabling (i) the discovery of high-redshift GRBs as well

as (ii) studying the prevalence of dust along GRB sightlines, i.e. quantifying the incidence of 'dark' bursts. Other scientific highlights include (iii) studies of Fermi-detected GRBs (including the redshift estimate of GRB 080916C), (iv) measurements of the SEDs of non-canonical light curve variability such as flares or intensity jumps, (v) the discovery and detailed study of a large fraction of all GRB-SNe, most prominently the SN 2011kl related to the ultra-long GRB 111209A, (vi) tests of the simplest fireball scenario based on the evolution of afterglow SEDs, (vii) the investigation of the jet structure and/or off-axis viewing geometry based on achromatic afterglow light curves, (viii) and the characterization of about half of all optically-detected short GRB afterglows. Beyond GRBs, the black widow binaries and photometric redshift estimates for blazars are the most noteworthy topics.

Over the years, the versatility of GROND has made it the instrument with the largest share of observing time among the three instruments at the 2.2m ESO/MPG telescope. This has been a rewarding experience for the team that designed and built the instrument. It also demonstrates that specialized instruments with unique capability at a small telescope can indeed make competitive contributions in the era of 8-10m telescopes, and likely also in the upcoming era of even larger telescopes.

*I particularly acknowledge U. Laux for the mastery of the optical design of GROND, and S. Klose (both Thüringer Landessternwarte Tautenburg) for the long-standing fruitful collaboration since the early time of the development of GROND, as well as T. Krühler (formerly MPE) for his unprecedented breadth of technical and scientific insight, which substantially contributed to shape the success of GROND. I'm grateful for the enthusiasm and help of all the GRB-GROND team members over the years: P.M.J. Afonso, J. Bolmer, C. Clemens, C. Delvaux, J. Elliott, R. Filgas, J.F. Graham, D.A. Kann, F. Knust, A. Küpcü Yoldaş, M. Nardini, A. Nicuesa Guelbenzu, F. Olivares E., N. Primak, A. Rossi, P. Schady, S. Schmidl, T. Schweyer, G. Szokoly, I. Steiner, V. Sudilovsky, M. Tanga, C.C. Thöne, K. Varela, P. Wiseman, and A. Yoldaş. I appreciate rewarding discussions with D.H. Hartmann, M. Ajello, B. Stecklum, H. van Eerten, L. Mancini, B. Biller, and E. Banados, and the always instant support by the ESO La Silla crew in all circumstances. Paulo M.J. Afonso (now at the American River College, U.S.A.) identified the very red object described in sect. 6.3, leading to the VLT follow-up spectroscopy. Part of the funding for GROND (both hardware as well as personnel) was generously granted from the Leibniz-Prize (DFG grant HA 1850/28-1) to Prof. G. Hasinger. Additional funding was provided by the Thüringer Landessternwarte Tautenburg.*

*Facilities:* Max Planck:2.2m, GROND instrument.

## REFERENCES

- Abbott B.P., Abbott R., Abbott T.D. et al. 2017a, PRL 119, 161101
- Abbott B.P., Abbott R., Abbott T.D. et al. 2017b, ApJ,L 848, L12
- Abdollahi S., Ackermann M., Ajello M. et al. 2017, ApJ, 846, 34
- Akitaya H., Moritani Y., Ui T., et al. 2014, SPIE 9147, 91474

- Alexander K.D., Laskar T., Berger E., et al. 2017, *ApJ*, 848, 69
- Allard F., Homeier D., & Freytag B., 2012, *RSPTA*, 370, 2765
- Aloy M.A., Janka H.-T., & Müller E., 2005, *A&A* 436, 273
- Banados E., Venemans B.P., Morganson E., et al. 2014, *AJ*, 148, 14
- Banados E., Venemans B.P., Decarli R., et al. 2016, *ApJS* 227, 11
- Beletic J.W., Gerdes R., & Duvarney R.C., 1998, *Proc. ESO CCD workshop, Garching, 8-10 Oct. 1996*, Eds. J.W. Beletic and P. Amico, Kluwer, *ASSL* 228, p. 103
- Bernardes D.V., Martioli E., Rodrigues C.V., 2018, *PASP* 130, pp. 095002
- Biller B., Crossfield I.J.M., Mancini L. et al. 2013, *ApJ*, 778, L10
- Bottacini E., Ajello M., Greiner J. et al. 2010, *A&A*, 509, A69
- Burgasser A.J., Geballe T.R., Leggett S.K. et al. 2006, *ApJ*, 637, 1067
- Burgess J.M., Greiner J., Begue D., et al., 2017, [arXiv:1710.05823](https://arxiv.org/abs/1710.05823)
- Burningham B., Leggett S.K., Homeier D. et al. 2011, *MN* 414, 3590
- Butler N., Klein C., Fox O. et al. 2012, *SPIE* 8446, 844610
- Cameron A.C., 2016, in “Methods of Detecting Exoplanets”, *ASSL* 428, Springer, 89
- Cano Z., de Ugarte Postigo A., Pozanenko A., et al. 2014, *A&A*, 568, A19
- Cano Z., Wang S.-Q., Dai Z.-G., & Wu X.-F., 2017, *Adv. Astron.*, ID 8929054
- Cappelluti N., Ajello M. Rebusco P., et al. 2009, *A&A*, 495, L9
- cenko S.B., Frail D.A., Harrison F.A., et al. 2010, *ApJ*, 711, 641
- cenko S.B., Frail D.A., Harrison F.A., et al. 2011, *ApJ*, 732, 29
- cenko S.B., Krimm H.A., Horesh A., et al. 2012, *ApJ*, 753, 77
- Chabrier G., Johansen A., Janson M., & Rafikov R., 2014, in “Protostars and Planets VI”, eds. H. Beuther et al., Univ. Arizona Press, p. 619
- Chandra, P., cenko, S.B., Frail, D.A., et al. 2008, *ApJ*, 683, 924
- Chen G., van Boekel R., Madhusudhan N. et al. 2014, *A&A*, 564, A6
- Chrimes A., Stanway E., Levan A. et al. 2018, *MN*, 478, 2
- Christille J.M., Bonomo A.S., Borsa F. et al. 2016, *SPIE* 9908, id. 990857
- Connelley M., Tokunaga A., Bus S., 2013, *AAS DPS meeting #45*, id. 211.12
- Costa E., Frontera F., Heise J., et al., 1997, *Nat.*, 387, 783
- Crossfield I.J.M., Biller B., Schlieder J.E. et al. 2014, *Nat.*, 505, 654
- Cucchiara A., Levan A.J., Fox D.B. et al. 2011, *ApJ*, 736, 7
- Depoy D., 1998, URL [www.astronomy.ohio-state.edu/~depoy/research/instrumentation/andicam/andicam.html](http://www.astronomy.ohio-state.edu/~depoy/research/instrumentation/andicam/andicam.html)
- Dhillon V.S., Marsh T.R., Stevenson M.J., et al., 2007, *MN* 378, 825
- Djorgovski S.G., Frail D.A., Kulkarni S.R., et al. 2001, *ApJ*, 562, 654
- Dunham E.W., Elliot J.L., Bida T.A., et al. 2004, *SPIE* 5492, 592
- Eliasdóttir Á., Fynbo J.P.U., Hjorth J., et al. 2009, *ApJ*, 697, 1725
- Elliott J., Greiner J., Khochfar S., et al., 2012, *A&A*, 539, A113
- Ellis T.A., Drake R., Fowler A.M., et al. 1993, in “Cryogenic Optical Systems and Instruments V”, *Proc. SPIE* 1765, 94
- Fan Y.-Z., Yu Y.-W., Xu D., et al. 2013, *ApJ*, 779, L25
- Filgas R., Krühler T., Greiner J. et al. 2011a, *A&A*, 526, A113
- Filgas R., Greiner J., Schady P. et al. 2011b, *A&A*, 535, A57
- Filgas R., Greiner J., Schady P. et al. 2012, *A&A*, 546, A101
- Fox D.B., Frail D.A., Price P.A. et al. 2005, *Nat.*, 437, 845
- Fruchter A.S., Levan A.J., Strolger L. et al. 2006, *Nat.*, 441, 463
- Fukugita M., Ichikawa T., Gunn J.E. et al. 1996, *AJ*, 111, 1748
- Fynbo J.U., Jensen B.L., Gorosabel J. et al. 2001, *A&A*, 369, 373
- Galama T.J., Vreeswijk P.M., van Paradijs J. et al. 1998, *Nat.*, 395, 670
- Gehrels N., Chincarini G., Giommi P., et al. 2004, *ApJ*, 611, 1005
- Gendre B., et al. *ApJ*, 766, A30

- Goldman B., Marsat S., Henning T., Clemens C., & Greiner J., 2010, *MN*, 405, 1140
- Golenetskii S., et al. *GCN Circ.* 12663, <http://gcn.gsfc.nasa.gov/gcn/gcn3/12663.gcn3>
- Gorosabel J., Ugarte Postigo A., 2010, in *Proc. of "High Time Resolution Astrophysics IV - The era of extremely large telescopes"*, Crete, May 2010, *PoS* 108, id. 36
- Graham J.F., & Fruchter A.S., 2017, *ApJ*, 834, 170
- Granot J., Panaitescu A., Kumar P., & Woosley S.E., 2002, *ApJ*, 570, L61
- Granot J., & Kumar P., 2003, *ApJ*, 591, 1086
- Greiner J., Clemens C., Krühler T., et al. 2007, *GCN Circ.* 6449, <http://gcn.gsfc.nasa.gov/gcn/gcn3/6449.gcn3>
- Greiner J., Bornemann W., Clemens C., et al. 2008, *PASP*, 120, 405
- Greiner J., Krühler T., Fynbo J.P.U., et al. 2009a, *ApJ*, 693, 1610
- Greiner J., Krühler T., McBreen S., et al. 2009b, *ApJ*, 693, 1912
- Greiner J., Krühler T., Klose S. et al., 2011, *A&A*, 526, A30
- Greiner J., Krühler T., Nardini M. et al. 2013, *A&A*, 560, A70
- Greiner J., Mazzali P.A., Kann D.A. et al. 2015, *Nat.*, 523, 189
- Greiner J., Delvaux C., Wyrzykowski L., et al. 2016, *Astron. Tel.* #8579
- Greiner J., Bolmer J., Wieringa M. et al. 2018, *A&A*, 614, A29
- Groot P.J., Galama T.J., van Paradijs J., et al. 1998, *ApJ*, 493, L27
- Gvaramadze V.V., Langer N., Fossati L., et al. 2017, *Nat. Astron.*, 1, 0116
- Hjorth J., Sollermann J., Moller P. et al. 2003, *Nat.*, 423, 847
- Inserra, C., 2013, *ApJ*, 770, A128
- Jewitt D.C., 2002, *AJ*, 123, 1039
- Jha S., Charbonneau D., Garnavich P.M. et al. 2000, *ApJ*, 540, L45
- Kann D.A., Schady P., Olivares E. F., et al. *A&A* 617, A122
- Kasen, D., & Bildsten, L., *ApJ*, 717, 245
- Kasen D., Badnell N. R., & Barnes J., 2013, *ApJ*, 774, 25
- Kaur A., Rau A., Ajello M., et al. 2017, *ApJ*, 834, 41
- Katz J.I., 1994, *ApJ*, 422, 248
- Kennea J.A., 2015, *JHEAp*, 7, 105
- Kirkpatrick J.D., Cushing M.C., Gelino C.R. et al. 2011, *ApJS*, 197, 19
- Kleiser I.K.W., et al. 2011, *MN*, 415, 372
- Klose S., Stecklum B., Masetti N., et al. 2000, *ApJ*, 545, 271
- Klose S., Schmidl S., Kann D.A. et al. 2018, *A&A*, in press [arXiv:1808.02710]
- Knust F., Greiner J., van Eerten H., et al. 2017, *A&A*, 607, A84
- Komossa S., Zhou H., Rau A., et al. 2009, *ApJ*, 701, 105
- Komossa S., 2017, *AN* 338, 256
- Kotani T., Kawai N., Yanagisawa K., et al. 2005, *Il Nuovo Cim.* 28 C, p. 755 (astro-ph/0702708)
- Krühler T., Küpcü Yoldaş A., Greiner J., et al. 2008, *ApJ*, 685, 376
- Krühler T., Greiner J., McBreen S., et al. 2009a, *ApJ*, 697, 758
- Krühler T., Greiner J., Afonso P., et al. 2009b, *A&A*, 508, 593
- Krühler T., Schady P., Greiner J. et al. 2011a, *A&A*, 526, A153
- Krühler T., Greiner J., Schady P., et al. 2011b, *A&A*, 531, A108
- Kumar P., & Piran T., 2000, *ApJ*, 535, 152
- Lamb D.Q., & Reichart D.E., 2000, *ApJ*, 536, 1
- Laskar T., Berger E., Tanvir N.R., et al. 2014, *ApJ*, 781, 1
- Lattimer J.M., & Prakash M., 2011, in "From Nuclei to Stars", ed. S. Lee, World Scientific, p. 275
- Lazzati D., Covino S., & Ghisellini G., 2002a, *MN*, 330, 583
- Lazzati D., Rossi E., Covino S., Ghisellini G., & Malesani D., 2002, *A&A*, 396, L5
- Le T., & Mehta V., 2017, *ApJ*, 837, 17
- Lendl M., Afonso C., Koppenhoefer J. et al. 2010, *A&A*, 522, A29
- Levan A., et al. *ApJ*, 781, A13
- Lipunov V.M., Postnov K.A., & Prokhorov M.E., 2001, *Astron. Rep.* 45, 236
- Lodato G., Franchini A., Bennerot C., & Rossi E.M., 2015, *JHEAp* 7, 158
- Luhman K.L., 2013, *ApJ*, 767, L1
- Lunnan, R., et al. 2013, *ApJ*, 771, A97
- Mancini L., Nikolov N., Southworth J., et al. 2013, *MN*, 430, 2932
- Mancini L., Southworth J., Ciceri S., et al. 2014, *A&A*, 568, A127



- Mazzucchelli C., Banados E., Venemans B.P., et al. 2017, *ApJ*, 849, 91
- McBreen S., Krühler T., Rau A. et al. 2010, *A&A*, 516, A71
- Mereghetti S., Paizis A., Götz D., et al. 2010, *GCN Circ.* 10555, <http://gcn.gsfc.nasa.gov/gcn/gcn3/10555.gcn3>
- Merloni A., Dwelly T., Salvato M., et al. 2015, *MN*, 452, 69
- Meszáros P., & Rees M.J., 1997, *ApJ*, 476, 232
- Metzger B.D., Martínez-Pinedo G., Darbha S., et al. 2010, *MN*, 406, 2650
- Meyer M., Finger G., Mehrgan H., et al. 1998, in *Proc. "Infrared Astronomical Instrumentation"*, ed. A.M. Fowler, *SPIE Vol. 3354*, p. 134
- Möhler-Fischer M., Mancini L., Hartman J.D., et al. 2013, *A&A*, 558, A55
- Mookerjea B., Parisi P., Bhattacharyya S., et al. 2010, *MN*, 409, L114
- Nakauchi D., Kashiyama K., Suwa Y., & Nakamura T., *ApJ*, 778, A67
- Nardini M., Greiner J., Krühler T., et al. 2011, *A&A*, 531, A39
- Nardini M., Elliott J., Filgas R., et al. 2014, *A&A*, 562, A29
- Negoro H. and MAXI team, 2017, in "7 years of MAXI", *Proc. conf. Dec. 2016*, p. 15 (online at [http://maxi.riken.jp/conf/sevenyears/pdf/O\\_03.pdf](http://maxi.riken.jp/conf/sevenyears/pdf/O_03.pdf))
- Nicuesa Guelbenzu A., Klose S., Rossi A., et al. 2011, *A&A*, 531, L6
- Nicuesa Guelbenzu A., Klose S., Greiner J., et al. 2012, *A&A*, 548, A101
- Olivares Estay F., Greiner J., Schady P. et al. 2012, *A&A*, 539, A76
- Olivares Estay F., Greiner J., Schady P. et al. 2015, *A&A*, 577, A44
- Orosz J.A., & Bailyn C.D., 1997, *ApJ*, 477, 876
- Paczynski B., 1986, *ApJ*, 304,1
- Paczynski B., & Rhoads J., 1993, *ApJ*, 418, L5
- Panaiteescu A., Mészáros P., & Rees M., 1998, *ApJ*, 503, 314
- Panaiteescu A., & Kumar P., 2002, *ApJ*, 571, 779
- Pian, E. et al. 2006, *Nat.*, 442, 1011
- Pierini D., Suhada R., Fassbender R., et al. 2012, *A&A*, 540, A45
- P2PP (Phase2 Proposal Preparation) Manual, 2007, v. 2.13, Issue 9, Doc. No. VLT-MAN-ESO-19200-1644
- Rau A., Schady P., Greiner J. et al. 2012, *A&A*, 538, A26
- Rau A., extracted from [http://www.mpe.mpg.de/~arau/GRBs\\_bonn.pdf](http://www.mpe.mpg.de/~arau/GRBs_bonn.pdf)
- Rees M.J., & Meszaros P., 1998, *ApJ*, 496, L1
- Reif K., Bagschik K., de Boer K.S., et al., 1999, *SPIE* 3649, 109
- Rhoads J.E., 1999, *ApJ*, 525, 737
- Rodrigues C.V., Taylor K., Jablonski F. et al. 2012, *SPIE* 8446, 844626
- Romani R.W., Filippenko A.V., Silverman J.M. et al. 2012, *ApJ*, 760, L36
- Romani R.W., Filippenko A.V., & Cenko S.B., 2015, *ApJ*, 804, 115
- Roming P.W.A., Vanden Berk D., Pal'shin V., et al. 2006, *ApJ*, 651, 985
- Roming P.W.A., van der Horst A., OCTOCAM Team, 2018, *AAS Meeting #231*, id. 314.06
- Rossi A., Klose S., Ferrero P., et al. 2012, *A&A*, 545, A77
- Salvetti D., Mignani R.P., De Luca A. et al. 2015, *ApJ*, 814, 88
- Salvetti D., Mignani R.P., De Luca A. et al. 2017, *MN*, 470, 466
- Sari R., & Piran T., 1997, *ApJ*, 485, 270
- Sauer, D.N. et al. 2006, *MN*, 369, 1939
- Selsing J., Fynbo J.P.U., Christensen L., & Krogager J.-K., 2016, *A&A*, 585, A87
- Smartt S.J., Chen T.-W., Jerkstrand A., et al. 2017, *Nat.*, 551, 75
- Snellen I.A.G., Koppenhöfer J., van der Burg R.F.J., et al. 2009, *A&A*, 497, 545
- Spano P., De Caprio V., La Foresta M. et al. 2010, *Proc. SPIE* 7735, id. 773565
- Stamatellos D., 2017, in "Star formation from cores to clusters", *Proc. conf. Santiago, March 2017*, id. 56 (online at <http://www.eso.org/sci/meetings/2017/star-formation2017.html>)
- Stanek, K.Z., Matheson T., Garnavich P.M. et al. 2003, *ApJ*, 591, L17
- Stone N.C., Kesden M., Cheng R.M., & van Velzen S., 2018, *Gen. Relativ. and Grav.*, submitted, [arXiv:1801.10180]
- Stratta G., D'Avanzo P., Piranomonte S., et al. 2007, *A&A*, 474, 827
- Tanvir N.R., Fox D.B., Levan A.J. et al. 2009, *Nat.*, 461, 1254
- Taubenberger S., Pastorello A., Mazzali P.A., et al. 2006, *MN*, 371, 1459
- Teplitz H.I., Malumuth E., Woodgate B.E. et al. 2000, *PASP*, 112, 1188

- Updike A., Rau A., Olivares E.F., & Greiner J., 2010, GCN Circ. 10558, <http://gcn.gsfc.nasa.gov/gcn/gcn3/10558.gcn3>
- van Paradijs J., Groot P.J., Galama T., et al., 1997, Nat., 386, 686
- Varela K., van Eerten H., Greiner J. et al., 2016, A&A, 589, A37
- Varela K., 2017, PhD thesis, TU Munich
- Venemans B.P., Banados E., Decarli R., et al. 2015, ApJ, 801, L1
- Vlasis A., van Eerten H.J., Meliani Z., & Keppens R., 2011, MN, 415, 279
- Wang X., & Loeb A., 2000, ApJ, 535, 788
- Watanabe M., Nakaya H., Yamamuro T., et al., 2005, PASP, 117, 870
- Wijers R.A.M.J., et al. 1997, MN, 288, L51
- Wijers R.A.M.J., & Galama T., 1999, ApJ, 523, 177
- Wosley S.E., Eastman R.G., & Schmidt B.P., 1999, ApJ, 516, 788
- Wyrzykowski L., Kostrzewa-Rutkowska Z., Udalski A., et al. 2016, Astron. Tel. #8577
- Wyrzykowski L., Zieliński M., Kostrzewa-Rutkowska Z., et al. 2017, MN, 465, L114
- Yates R., Kann D.A., Delvaux C., & Greiner J., 2015, GCN Circ. 18674, <http://gcn.gsfc.nasa.gov/gcn/gcn3/18674.gcn3>
- Yost S.A., Harrison F.A., Sari R., & Frail D.A., 2003, ApJ, 597, 459